ACS APPLIED ENERGY MATERIALS

www.acsaem.org Article

Effect of Molecular Structure of Quinones and Carbon Electrode Surfaces on the Interfacial Electron Transfer Process

Graziela C. Sedenho, Diana De Porcellinis, Yan Jing, Emily Kerr, Luis Martin Mejia-Mendoza, Álvaro Vazquez-Mayagoitia, Alán Aspuru-Guzik, Roy G. Gordon, Frank N. Crespilho,* and Michael J. Aziz*

Cite This: *ACS Appl. Energy Mater.* 2020, 3, 1933−1943 Read Online

ACCESS | Metrics & More | Article Recommendations | Supporting Information

ABSTRACT: Quinones can undergo thermodynamically reversible proton-coupled electron transfer reactions and are being applied as electroactive compounds in aqueous organic batteries. However, the electrochemical reversibility of these compounds is affected not only by their molecular structure but also by the properties of a carbon-based electrode surface. This study combines experimental and theoretical approaches to understand this dependence. We study the electron transfer kinetics of two synthesized quinone derivatives and two commercially available ones with a glassy carbon, a highly ordered pyrolytic graphite, and a high-edge-density graphite electrode (HEDGE). The electrochemical reversibility is notably improved on the HEDGE, which shows a higher density of defects and presents oxygenated functional groups at its surface. The electron transfer kinetics are controlled by adsorbed species onto the HEDGE. Molecular dynamics simulation and quantum mechanics calculations suggest defects with oxygen-containing functional groups, such as C−O and C═O, on HEDGE surfaces drive the interaction with the functional groups of the molecules, during physisorption from van der Waals forces. The presence of sulfonic acid side groups and a greater number of aromatic rings in the molecular structure may contribute to a higher stabilization of quinone derivatives on HEDGEs. We propose that high-performance carbon-based electrodes can be obtained without catalysts for organic batteries, by the engineering of carbon-based surfaces with edge-like defects and oxygenated functional groups.

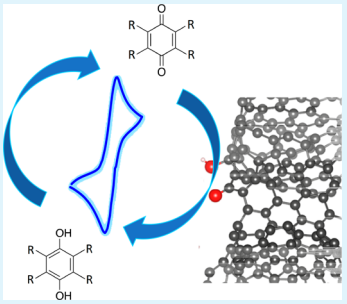

KEYWORDS: *quinones, carbon-based electrodes, graphite electrode, edge-plane-like defects, aqueous organic batteries, electrochemical reversibility, electron transfer kinetics*

1. INTRODUCTION

The generation of electrical energy from renewable sources, particularly wind and solar, is assuming increasing importance in modern society and can contribute to the worldwide expansion of the electric power generating capacity. However, to effectively use this renewable energy, it is necessary to deal with the inherent intermittency of these natural sources.[1] Methods for storing electrical energy could overcome this issue. Redox flow batteries (RFBs) have been recognized as a promising technology for large-scale energy storage.[2] In a RFB system, redox-active compounds are dissolved in electrolytes and separately stored in external tanks. The electroactive species are pumped between the reservoirs and the cell, where they are reversibly oxidized and reduced on the electrodes, storing or generating electricity that flows through an external circuit.[2] The performance of RFBs depends on several chemical, physical, and engineering factors, including the choice of redox compounds, electrode materials, membrane characteristics, and cell configuration.[1,2] Vanadium is the most popular electroactive species employed in commercial RFBs; however, the geographically limited supplies and high and fluctuating cost of this metal limit the widespread use of vanadium-based RFBs.[3] Quinone derivatives are interesting redox-active compounds in energy systems, such as in enzymatic biofuel cells[4−6] and in aqueous organic RFBs (AORFBs).[7−10] Quinone based molecules have been explored as alternative electroactive compounds in aqueous organic AORFBs because they are entirely composed of Earth-abundant elements and can be low cost and safe for use in residential and commercial environments.[7−10]

Quinone-based molecules can show thermodynamically reversible proton-coupled electron transfer reactions in acidic conditions.[11,12] However, the electrode material and its microstructure may also play a crucial role in affecting the electrochemical response and consequently the AORFB performance. Carbon-based electrodes have been widely employed in aqueous and nonaqueous RFBs because they show high electronic conductivity, high chemical and electrochemical stability, high specific surface area, and low cost.[13] A variety of carbon materials have been used in RFBs, such as

Received: December 5, 2019
Accepted: January 28, 2020
Published: January 28, 2020

https://dx.doi.org/10.1021/acsaem.9b02357
ACS Appl. Energy Mater. 2020, 3, 1933−1943

Scheme 1. Chemical Structure and Redox Reactions of (a) FQ, (b) CQ, (c) BQDS, and (d) ARS in Strongly Acidic Condition (pH ≈ 0)

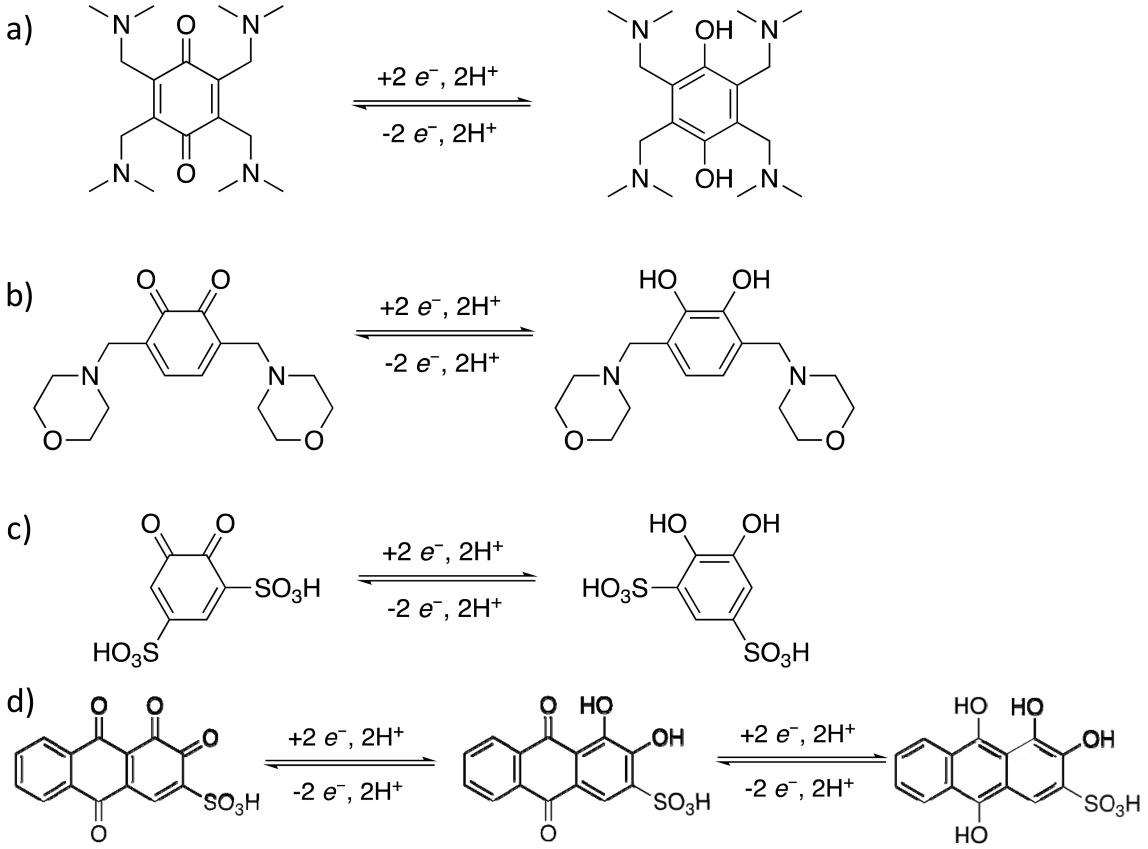

carbon papers[8−10,14−20] and graphitic felts.[21−24] Usually, these materials are submitted to thermal[8,9,15,17,19,23] or chemical treatments[10,14,15,20] or modification with nanomaterials[22,24,25] to improve wettability and electrochemical performance.

The effects of chemical and thermal treatments on the electrode have been extensively discussed in the literature in the context of vanadium RFBs.[26−28] Generally, the presence of edge-plane-like defects and oxygenated functional groups is reported to influence electrode performance in vanadium redox reactions.[26−28] However, in the context of AORFBs, the literature is lacking any information about how carbon-based electrode materials can influence the electrochemical behavior of organic molecules, such as quinones. Glassy carbon (GC) electrodes have been widely used to study the redox reactions of quinone molecules that exhibit Nernstian behavior in quiescent solution,[7−10,16,17] before testing the quinones in full cells. In this paper we show that some quinones exhibit electrochemical behavior strongly dependent on the carbon material structure.

To gain a better understanding of the quinone and carbon-based electrode system, we studied how carbon-based material surfaces can influence the electrochemical kinetics of quinone derivatives in quiescent solution. We evaluated the separation between anodic and cathodic peaks in cyclic voltammetry and determined adsorbed quinone surface excesses. We used molecular dynamics simulation and density functional theory (DFT) calculations to have atomistic insights and evaluate the adsorption energy at the quinone−carbon electrode surface interface. We used three carbon materials with distinct surface structure and composition: GC, highly ordered pyrolytic graphite (HOPG), and high-edge-density graphite electrode (HEDGE). We studied the electrochemical behavior of four different quinone derivatives with these electrodes. We selected molecules that are candidates to be used as posolytes (positive electrolyte) or in symmetrical AORFBs. We included benzoquinone- and anthraquinone-based compounds functionalized with sulfonic acid, hydroxyl, and amine groups. To interpret the experimental results, we modeled the interaction between quinone derivatives and carbon surfaces using molecular dynamics simulations and quantum mechanics calculations. This work contributes new insights into how carbon-based materials can be tuned to obtain electrodes with superior performance in semisolid AORFBs and solid-batteries involving adsorbed redox-active species. The presence of functionalities and microstructure of carbon-based electrodes should be carefully considered in electrochemical systems that involve redox processes of species in solution: although adsorption enhances the electron transfer kinetics, if it is too strong, however, it is expected to suppress the mass transfer kinetics. Therefore, this study benefits the fields of materials science and electrochemical energy storage.

2. RESULTS AND DISCUSSION

2.1. Molecular Electrochemistry of Quinones on Different Carbon-Based Surfaces. We studied the electrochemical behavior of four different quinone derivatives that are of interest for application in AORFBs. We synthesized two of these compounds: 2,3,5,6-tetrakis((dimethylamino)methyl)-benzene-1,4-diol (FQH_2) and 3,6-bis(morpholinomethyl)-cyclohexa-3,5-diene-1,2-diol (CQH_2). Their oxidized forms

https://dx.doi.org/10.1021/acsaem.9b02357
ACS Appl. Energy Mater. 2020, 3, 1933−1943

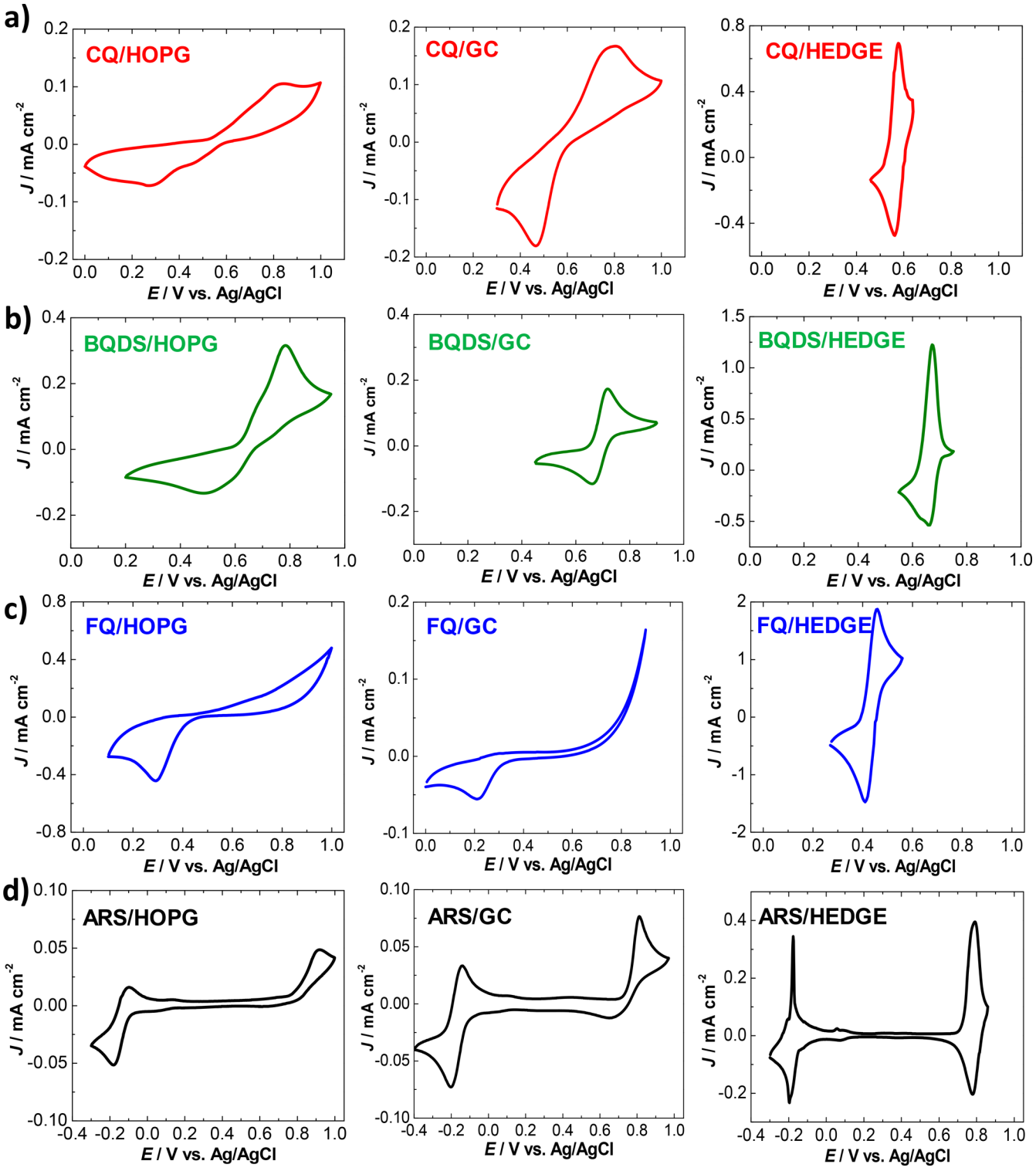

Figure 1. CVs (third cycle) of GC, HOPG, and HEDGE in 1.0 mol L^{-1} H_2SO_4 containing (a) 1.0 mmol L^{-1} CQ, (b) 1.0 mmol L^{-1} BQDS, (c) 10.0 mmol L^{-1} FQ, and (d) 1.0 mmol L^{-1} ARS. Scan rate: 50 mV s^{-1} (for FQ, CQ, and BQDS) and 5 mV s^{-1} (for ARS). Reference electrode is Ag/AgCl in 3 mol L^{-1} NaCl.

are 2,3,5,6-tetrakis((dimethylamino)methyl)cyclohexa-2,5-diene-1,4-dione, which we call frog quinone (FQ), and 3,6-bis(morpholinomethyl)cyclohexa-3,5-diene-1,2-dione, which we call crab quinone (CQ). The other two are commercial compounds: 1,2-dihydroxybenzene-3,5-disulfonic acid (BQDS) and 3,4-dihydroxy-9,10-dioxoanthracene-2-sulfonic acid, called Alizarin red S (ARS). The structures of all four molecules in their oxidized and reduced forms are shown in Scheme 1.

FQ is a *p*-benzoquinone functionalized with four trimethylamine groups (see structure in Scheme 1).[29] FQ is cheap and easy to synthesize (Section 1, Supporting Information). CQ is an *o*-benzoquinone and has attached two heterocyclic structures with morpholine groups. This compound (Section

https://dx.doi.org/10.1021/acsaem.9b02357
ACS Appl. Energy Mater. 2020, 3, 1933−1943

2, Supporting Information) was previously reported as a precursor for the synthesis of antioxidants.[30] However, this molecule has never been used in an AORFB. BQDS is a commercial *o*-benzoquinone functionalized with two sulfonic acid groups; it was previously reported as the active material in an AORFB posolyte.[16] The presence of electron-withdrawing side groups in FQ, CQ, and BQDS shifts the reduction potentials to higher values when compared to the analogous nonfunctionalized compounds.[12,31] The relatively high reduction potentials of these compounds make them candidates for application in the posolyte of an AORFB. Similar to previous work about quinone derivatives in strongly acidic conditions (pH ≈ 0),[7,10,16] FQ, CQ, and BQDS are expected to show a rapid and reversible reduction of quinone to hydroquinone form by transfer of two protons and two electrons on electrodes.

ARS is a *p*-anthraquinone derivative having additionally an 3,4-hydroquinone motif and one sulfonic acid group attached to the molecular skeleton. ARS contains both electron−proton donor hydroxyl groups and electron−proton acceptor carbonyl groups. Therefore, ARS exhibits three redox states instead of two, as shown in Scheme 1. Consequently, ARS has been considered for use as both a posolyte and negolyte of the same AORFB.[32,33]

It is well-known that the structure of carbon electrodes and the presence of functionalities influence the electron transfer kinetics of several redox reactions.[28,34−38] Here, we present a series of experiments designed to probe the effect of the electrode surface on quinone electrochemistry. For that, three carbon-based electrodes with distinctive features were used: GC, HOPG, and HEDGE. GC is a standard carbon-based electrode used to investigate the electrochemical behavior of redox-active compounds and to study new molecules for application in ORFBs.[4−7,14,18,36] Microscopic, spectroscopic, and diffraction studies[40,41] have revealed that GC mainly consists of curved carbon sheets that contain an sp^2-bonded network of hexagons interspersed with pentagons and heptagons. Models for GC show a predominance of nanosized graphite-like domains in its structure. These features are independent of the thermal treatment used in the GC production process.[40] In GC production, the material is subjected to high temperature that leads to a noticeable ordering of aromatic nanoclusters.[40] Thus, it is expected that the surface of GC has more edge-plane sites than HOPG but fewer edge-plane sites than HEDGE. The Raman spectrum of GC (Figure S5, Supporting Information) indicates that its structure contains nanosized disordered sp^2 domains, which is consistent with the literature.[40,41]

Differently, HOPG and HEDGE have graphitic structures, however, with very distinct characteristics. In HOPG, the graphene layers lie parallel to the surface; thus, this structure provides a basal plane surface with very few defects.[42] In contrast, HEDGE is produced in a way that exposes a high density of edge-plane-like defect sites on the surface, by manually polishing single-crystalline graphite at a large misorientation to the basal plane (Section 3, Supporting Information). Previous studies report that edge-plane carbon electrodes[35,43,44] improve the electrochemical kinetics of several compounds, including ascorbic acid,[36] nicotinamide adenine dinucleotide,[36,37] epinephrine,[37] quinones,[45,46] ferricyanide,[36,37] ferrocene derivatives,[35] and molecular oxygen.[38] Recently, the presence of defects on carbon electrodes has been shown to enhance the performance of vanadium[26−28,34] and zinc−bromine[14] RFBs.

In this context, the electrochemical behavior of the quinone derivatives was investigated by cyclic voltammetry (Section 3, Supporting Information) on HOPG, GC, and HEDGE, as shown in Figure 1. In Figure 1a, we can observe that the cyclic voltammogram (CV) of CQ recorded on HOPG exhibits a broad oxidation peak at 0.84 V and a major reduction peak at 0.27 V, with a large peak-to-peak separation (ΔE_p) of 570 mV. CV of CQ on GC shows broad oxidation and reduction peaks at 0.80 and 0.47 V, respectively, with a smaller ΔE_p, 330 mV, compared to HOPG. However, the wide values of ΔE_p indicates a quasi-reversible redox reaction on both HOPG and GC electrodes. In contrast, the CV of CQ on HEDGE shows a well-defined redox couple with half-wave potential ($E_{1/2}$) equal to 0.57 V and ΔE_p equal to 17 mV. This measured value of ΔE_p is smaller than the value of 30 mV expected for a reversible two-electron process involving freely diffusing species. This deviation suggests that the electron transfer process occurs between adsorbed species and the HEDGE surface.

Similarly to CQ, the CV of BQDS on HOPG (Figure 1b) also shows very broad oxidation and reduction peaks at 0.78 and 0.49 V, respectively, with ΔE_p equal to 290 mV. However, the CV of BQDS on GC shows a pair of well-defined redox peaks with $E_{1/2}$ equal to 0.69 V and ΔE_p of 57 mV, which suggests a quasi-reversible electrochemical reaction, as it involves two electrons. Also, CV of BQDS on HEDGE exhibits a well-defined redox couple at $E_{1/2}$ = 0.67 V. The small value of ΔE_p, 12 mV, suggests that the electron transfer process occurs by adsorbed species on the HEDGE surface. For FQ, a similar voltammetric profile (Figure 1c) is observed on HOPG and GC. On both electrodes, FQ does not show a well-defined oxidation peak; nevertheless, the onset oxidation current is observed at ∼0.5−0.6 V. In the reverse scan, a reduction peak is observed at 0.29 and 0.21 V on HOPG and GC, respectively. In contrast, reversible CV of FQ was notably obtained by using the HEDGE. FQ exhibits a pair of well-defined redox peaks at $E_{1/2}$ = 0.43 V with a ΔE_p of 43 mV, which is close to the value of 30 mV that characterizes a reversible one-step two-electron, two-proton redox reaction. With regard to ARS, the CVs (Figure 1d) show several redox processes, which are very similar on HOPG and GC. The first quasi-reversible redox couple has been assigned to the 9,10-quinone functionality[47,48] and appears at −0.14 V with ΔE_p equal to 80 mV on HOPG and at −0.17 V with ΔE_p equal to 63 mV on GC, indicating quasi-reversible redox reactions on those electrodes. On HEDGE, the same redox couple is observed at −0.19 V with ΔE_p of 21 mV. The second anodic peak of ARS is be attributed to the oxidation of 3,4-dihydroxyl groups[47,48] and appears at 0.92 V on HOPG and at 0.81 V on GC. However, the minuscule return peak at high potentials shows an irreversible redox reaction of the 1,2-oxygenated functional groups on HOPG and GC. In contrast, on the HEDGE, ARS presents a well-defined high-potential redox couple with $E_{1/2}$ of 0.78 V and ΔE_p of 11 mV. This result indicates a reversible redox reaction involving adsorbed species on the HEDGE surface. Reversible behavior for both redox couples of ARS has been previously reported by Tong et al.[33] The CV results indicate that the electron transfer kinetics of the different quinone derivatives is strongly affected by the structure of carbon electrode. We interpret the shapes of the CVs obtained with the HEDGE to mean that all quinones studied have fast

https://dx.doi.org/10.1021/acsaem.9b02357
ACS Appl. Energy Mater. 2020, 3, 1933−1943

electron transfer on edge sites of graphitic structures. This electron transfer rate is controlled by adsorbed species on the electrode surface, as shown by the values of ΔE_p and the linear correlation between the peak current densities and the scan rate (Figure S4). HEDGE exhibits an electrochemical surface area (ECSA) that is higher than that of HOPG by a factor of 29 (Section 9, Supporting Information); after normalization by ECSA, the faradaic currents obtained with the HEDGE remain higher than those obtained with HOPG. Therefore, we conclude that the higher faradaic current densities recorded on the HEDGE are not an area effect, but they are occasioned by the greater electrochemical kinetic rate constants. These observations warn that GC may not be the most appropriate electrode to evaluate the electrochemistry of new organic molecules in quiescent solution for subsequent application in AORFBs.[7−10,17,21,39] This may lead to discarding molecular candidates that would show rapid and reversible electron transfer kinetics at another carbon electrode.

2.2. Origin of Defects on the HEDGE Surface. To investigate the origin of the electrochemical behavior of quinones on defects on the HEDGE surfaces, we characterized the microstructure, morphology, and chemical composition of carbon-based electrodes using Raman spectroscopy, scanning electron microscopy (SEM), and X-ray photoelectron spectroscopy (XPS), respectively, as shown below (Sections 6−8, Supporting Information). Raman spectra of HOPG and HEDGE in Figures 2a and 2b, respectively, show the expected D- and G-bands centered at 1335 and 1581 cm^{-1}, respectively.

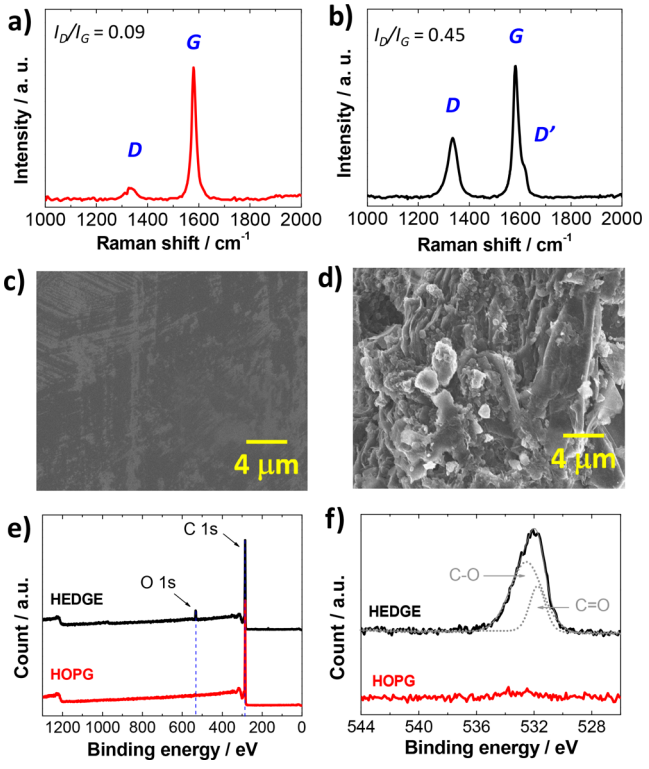

Figure 2. Raman spectra of HOPG (a) and HEDGE (b) obtained with 633 nm excitation laser. SEM images of HOPG (c) and HEDGE (d). XPS survey spectra (e) of HOPG and HEDGE and their high-resolution spectra in O 1s region (f), where solid red and solid black curves represent raw spectra of HOPG and HEDGE, respectively, and dotted gray lines and solid gray line represent respectively the deconvoluted peaks and the sum of the deconvoluted peaks.

The G-band is associated with the presence of the hexagonal sp^2 carbon network, whereas D-band is a defect-induced Raman feature that is forbidden in perfect graphite.[49,50] HOPG exhibits a sharp symmetry-allowed G-band and a very small defect-induced D-band, indicating highly crystalline graphite. In contrast, the Raman spectrum measured on the HEDGE presents a pronounced D-band as well as a D′-band at 1620 cm^{-1}. These bands are originated from two scattering processes consisting of one elastic scattering event by defects of the crystal and one inelastic scattering event by emitting or absorbing a phonon. The D-band originates from an intervalley double-resonance process, involving electronic states around two inequivalent K points in the Brillouin zone of graphite, whereas the D′-band originates from an intravalley double-resonance process involving electronic states around the same K point.[49] The ratio of the intensity of D- and G-bands (I_D/I_G) was used to quantify the defect densities in both electrodes. The I_D/I_G ratio of 0.45 for the HEDGE indicates more defects on the HEDGE compared to I_D/I_G of 0.09 for the HOPG electrode. As observed in SEM images (Figures 2c,d), the electrodes show drastic differences in terms of microstructure and morphology. The HOPG electrode (Figure 2c) exhibits a flat surface with few scratches, whereas the HEDGE (Figure 2d) has a densely packed microfractured surface. These SEM results are in agreement with the Raman spectroscopic results, where the presence of defects on the HEDGE is confirmed by the higher I_D/I_G ratio. Some authors have discussed the edge-plane-like defects on carbon materials in terms of the presence of oxygenated functional groups.[14,26−28,34] It is expected that the HEDGE presents more oxygen atoms on the surface compared with HOPG because the HEDGE is prepared by an abrasive procedure in atmospheric conditions to produce a high density of edge-plane-like defect sites on the surface (Section 3, Supporting Information).

To examine the presence of oxygenated functional groups in both HEDGE and HOPG electrodes, XPS measurements were performed. XPS wide scan surveys (Figure 2e) indicate the presence of carbon atoms on both electrode surfaces; however, oxygen atoms were detected only on the HEDGE surface. The high-resolution spectrum (Figure 2f) of HOPG shows a very small and broad peak at around 533 eV, which is related to oxygen; however, this signal is close to the level of background noise. This result is consistent with the Raman and SEM results, which indicate that there are very few defects on HOPG where oxygenated functional groups could form. The atomic ratio of oxygen to carbon (O/C) was considerably higher on the HEDGE (O/C = 0.069), as shown by the peak at 532 eV attributed to O 1s in Figure 2e. The type of oxygenated functional groups on the HEDGE can be determined by deconvolution of the high-resolution spectra in the O 1s region (Figure 2f). The deconvolution shows two peaks, which are assigned to C═O (531.8 ± 0.2 eV) and C−O (532.6 ± 0.2 eV).[51] Based on the area of deconvoluted peaks, the percentage of the oxygenated functional groups was calculated to be 66.3% of C−O and 33.7% of C═O. XPS results suggest that oxygen in the edge-plane structures is in the form of hydroxyl, ether, and carbonyl functional groups (see high-resolution XPS spectrum in the C 1s region in Figure S6).

2.3. Adsorption of Quinones on the HEDGE Surface. We have observed by CV that quinones can be adsorbed on the HEDGE surface; on the basis of that, we performed a detailed investigation on how the molecular structure of

https://dx.doi.org/10.1021/acsaem.9b02357
ACS Appl. Energy Mater. 2020, 3, 1933−1943

quinone-based molecules influences the adsorption phenomena. The amount of quinone adsorbed under applied overpotential conditions was measured by using anodic stripping voltammetry.[52] The details of the procedure can be found in Section 10 of the Supporting Information. FQ, CQ, BQDS, and ARS were first electroadsorbed from their solutions onto the HEDGE surface at high potential. After electroadsorption, the quinones (adsorbate) on the HEDGE surface were quantified by the faradaic current from the CVs, as shown in Figure 3a–d. To obtain the faradaic current, the

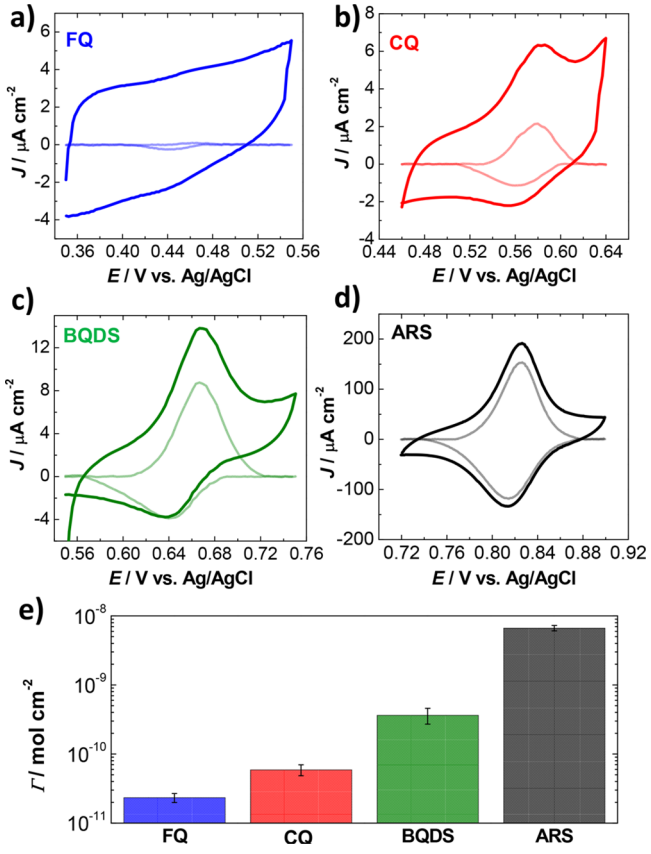

Figure 3. CVs recorded at 5 mV s^{-1} in 1.0 mol L^{-1} H_2SO_4 on HEDGE after electroadsorption of FQ (a), CQ (b), BQDS (c), and ARS (d). Thin lines: CVs after subtraction of the capacitive current. (e) Surface excess (Γ) of quinones on the HEDGE surface obtained from anodic peak of the first CV; the plot shows the mean Γ obtained from three HEDGE electrodes, and error values were obtained based on a *t*-distribution with 95% confidence interval.

capacitive current was subtracted from the original CVs, as shown in the insets of Figure 3a–d. Because the faradaic current is related to the quantity of adsorbed molecules (eqs S4 and S5, Supporting Information), the surface excess (Γ) of each quinone was determined (Section 10, Supporting Information) to be (2.3 ± 0.3) × 10^{-11}, (5.9 ± 1.0) × 10^{-11}, (3.6 ± 0.9) × 10^{-10}, and (6.7 ± 0.6) × 10^{-9} mol cm^{-2} for FQ, CQ, BQDS, and ARS, respectively. As shown in Figure 3e, the amount of adsorbed species follows the ascending order: FQ < CQ < BQDS < ARS.

The desorption process of FQ, CQ, BQDS, and ARS from the HEDGE surface was also investigated. For this, successive CVs of quinones previously adsorbed onto HEDGE were recorded in clean (without quinone) 1.0 mol L^{-1} H_2SO_4 electrolyte, as shown in Figure 4a–d. The desorption behavior is visualized by the plot of anodic faradaic peak current densities against the successive cycles, as shown in Figure 4e–h. Each quinone presents a different desorption profile, which suggests that molecular structure influences the interaction with the HEDGE surface. ARS is the only quinone that remains significantly adsorbed on the HEDGE surface after ~10 consecutive CVs. In contrast, FQ, CQ, and BQDS are rapidly released from the electrode surface, which is evidenced by the pronounced decay of the anodic peak current densities over successive CV cycles. These results suggest that these species possess different adsorption energies on HEDGE. Insight into the adsorption behavior and the molecular interaction between quinone-based molecules and HEDGE is provided by molecular dynamics and quantum mechanics simulations, as shown below.

2.4. Molecular Dynamics Simulation and DFT Calculations. We used molecular dynamics simulation and DFT calculations to model the interactions of FQ, CQ, BQDS, and ARS with a HEDGE surface (Section 11, Supporting Information). To simulate the HEDGE structure, we have used a melting–quenching–annealing schedule using NVT molecular dynamics with a Nosé–Hoover thermostat and Tersoff many-body potentials, which gives structures with different degrees of graphitization, defects, and orientations (Figure S10). Some C–C bonds were broken to introduce oxygenated functional groups, such as carbonyl and hydroxyl groups, based on XPS experimental results for HEDGE. The structure and geometry were optimized by using the QuantumESPRESSO (QE) package.

As previously reported,[53,54] this methodology provides accurate and optimized carbon structures with low computational cost, showing some advantages over other methodologies that employ a reverse Monte Carlo technique, which requires experimental data, or *ab initio* molecular dynamics, which is computationally expensive.[3]

After the simulation and optimization of the HEDGE structure, we investigated the interaction between this structure and the oxidized forms of ARS, BQDS, CQ, and FQ. Figure 5a–d shows the lowest energy configurations for the fully oxidized forms of FQ, CQ, BQDS, and ARS on a HEDGE surface containing C=O and C–O groups. The zoom view can identify which atoms of the quinone molecules are close to the HEDGE surface. The HEDGE–molecule distances shorter than 5 Å are highlighted in Figure 5a–d, as attractive forces between organic compounds and carbon surfaces can be significant up to this distance.[55] The lowest energy configuration shows the interaction between FQ and HEDGE surface (Figure 5a) probably occurs through the carbon (3.05 Å) and nitrogen (3.12 Å) atoms from the tertiary amine group and oxygen (4.65 Å) from the quinone functionality. For CQ (Figure 5b), the closest atoms to the carbon surface are carbon (3.49 Å) and oxygen (3.89 and 3.91 Å) atoms from C=O groups and nitrogen (4.73 Å) from the morpholine side group. In the case of BQDS (Figure 5c), the interaction with the surface possibly occurs through oxygen (2.77 and 3.28 Å) and sulfur (3.63 Å) atoms from sulfonic acid groups and carbon atoms (3.66 Å) from C=O groups. Similarly, sulfonic acid and carbonyl groups of ARS is also involved in the interaction with the HEDGE surface (Figure 5d) through the sulfur (4.48 Å), oxygen (2.89 and 3.17 Å), and carbon (2.91 Å) atoms. In addition, in all four systems studied here, oxygenated functional groups in the HEDGE structure are the closest regions to the molecules, suggesting they play

https://dx.doi.org/10.1021/acsaem.9b02357
ACS Appl. Energy Mater. 2020, 3, 1933–1943

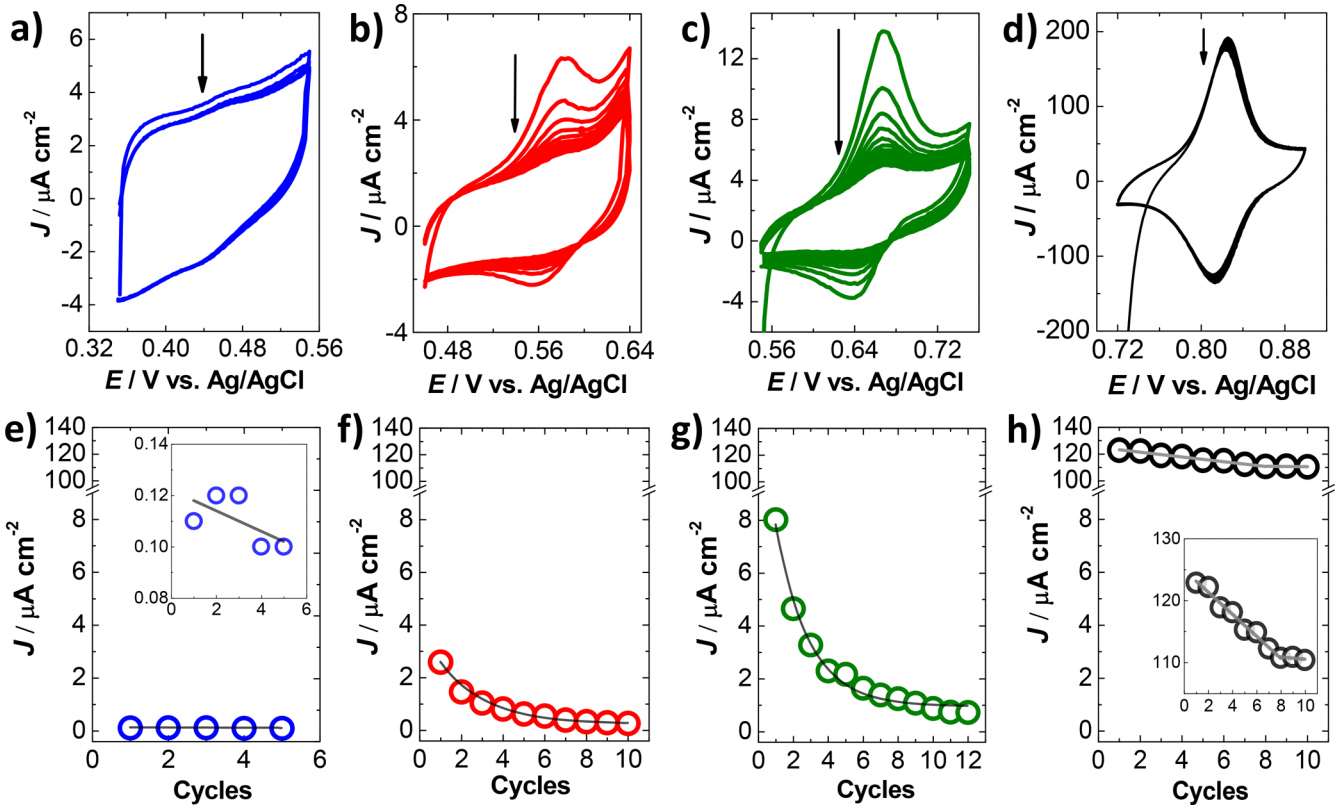

Figure 4. Successive CVs recorded at 5 mV s^{-1} in 1.0 mol L^{-1} H_2SO_4 on HEDGE after electroadsorption of FQ (a), CQ (b), BQDS (c), and ARS (d); the vertical arrows indicate the decrease in the anodic peak currents. Anodic peak current density over successive CVs after electroadsorption of FQ (e), CQ (f), BQDS (g), and ARS (h). Insets show zoomed-in views of the curves.

an important role in the attraction forces with the quinones. The molecule−surface distances indicate weak short-range van der Waals forces[56] are responsible for interaction, without forming chemical bonds. Otherwise, in the case of covalent bonds, molecule−surface distances would be expected to be smaller than 2 Å.[57]

The adsorption energy (ΔE_{ads}) of each molecule on the HEDGE surface in the lowest energy configuration was calculated by eq 1:

$$\Delta E_{ads} = E_{G+M} - E_G - E_M \quad (1)$$

where E_{G+M} is the geometry-optimized energy of the HEDGE surface with the molecule over it, E_M is the geometry-optimized isolated molecule inside the simulation box, and E_G is the geometry-optimized energy of the carbon surface in the simulation box. Based on these optimized configurations, ΔE_{ads} values were calculated to be −17.98, −19.10, −22.65, and −30.69 kcal mol^{-1}, for FQ, CQ, BQDS, and ARS, respectively (Figure 5e). ΔE_{ads} values represent the total adsorption energy of the molecules and are in good agreement with the three or four points of van der Waals interactions between the quinone derivatives and HEDGE surface, as shown in Figure 5a−d, implying that these molecules interact with a HEDGE surface by physisorption. In addition, the calculated ΔE_{ads} corroborates the experimental data of the surface excess (Figure 3e). Among the four studied quinones, ARS showed the highest value of ΔE_{ads}, which is consistent with the high surface excess observed experimentally. Likewise, FQ showed the lowest value of ΔE_{ads}, which is consistent with the lowest surface excess obtained.

The relationship between the experimental surface excess of the quinone-based molecules and the calculated ΔE_{ads} can be visualized in Figure 6. The $\Delta E_{ads}/kT$ values represent the adsorption energy per molecule entity, where k is Boltzmann's constant (0.001987 kcal mol^{-1} K^{-1}) and T is the absolute temperature (300 K). Figure 6 shows that a higher ΔE_{ads} per molecule leads to a higher quantity of adsorbed molecules observed in the electrochemical measurements. In addition, the presence of sulfonic acid groups in BQDS and ARS may contribute to a higher stabilization of these molecules on HEDGE surfaces, indicated by the higher ΔE_{ads} values per molecule entity, which lead to higher surface excesses. Also, the number of aromatic rings in the molecular structure seems to influence the adsorption process, as the anthraquinone ARS shows the highest ΔE_{ads} value per molecule entity and highest surface excess when compared to the benzoquinones FQ, CQ, and BQDS.

To distinguish the effect of edge-plane-like defects in the carbon structure and that of the oxygen-containing functional groups on quinone adsorption, we performed a computational simulation and calculations with a HEDGE structure without oxygen-containing functional groups (HEDGE-nO) using the same electronic parameters as in the previous ones (Section 12, Supporting Information). On HEDGE-nO, the preferred interaction sites of the four quinone-based molecules are the carbon atoms on the edges of the carbon structure (Figure S11). The molecules interact with the HEDGE-nO structure by the same functional groups observed with HEDGE, with the only difference being the closest atom of the functional group of FQ and ARS. The closest atoms to the HEDGE-nO surface are hydrogen from the tertiary amino group of FQ and oxygen

https://dx.doi.org/10.1021/acsaem.9b02357
ACS Appl. Energy Mater. 2020, 3, 1933−1943

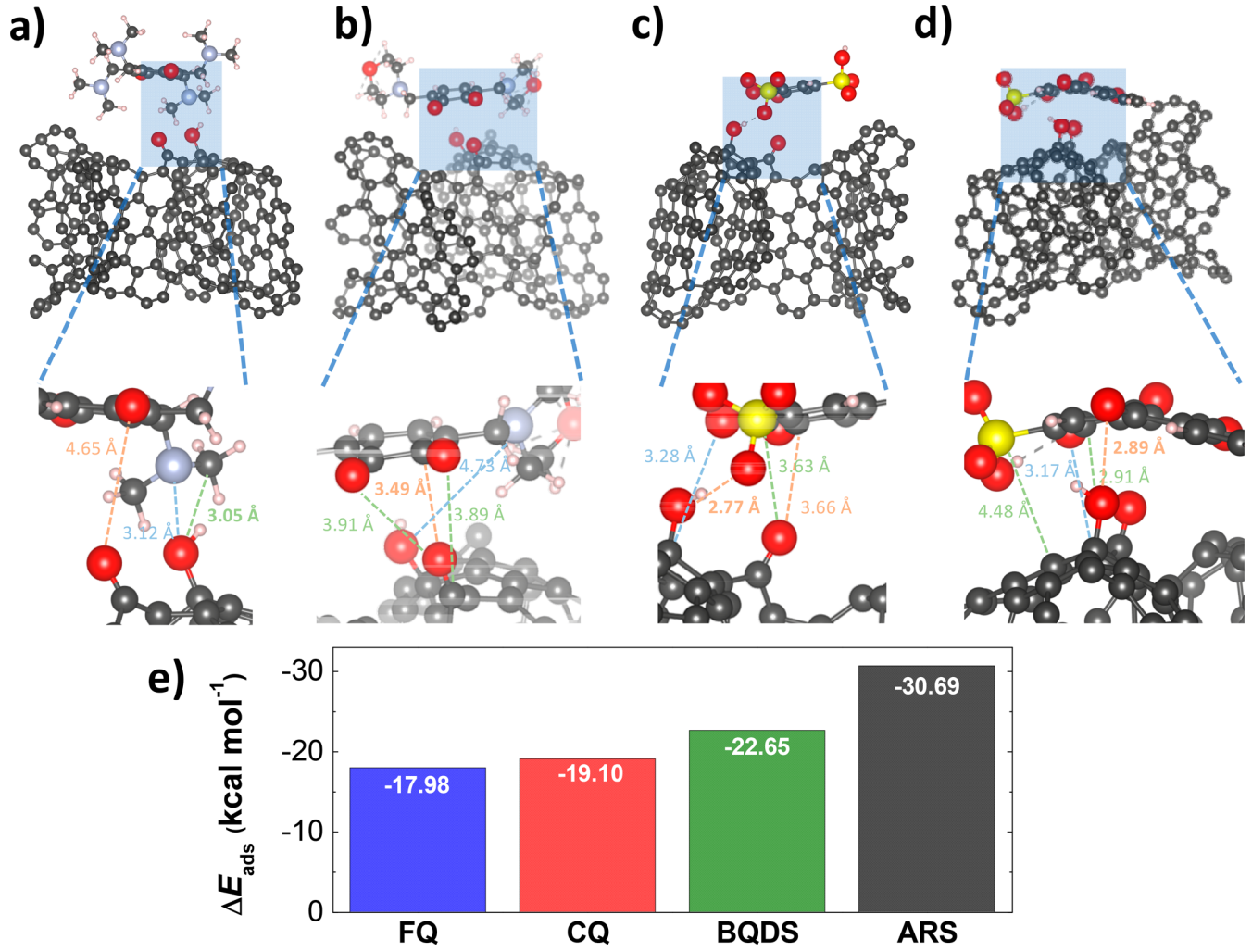

Figure 5. Lowest energy configurations of the fully oxidized form of FQ (a), CQ (b), BQDS (c), and ARS (d) on HEDGE. The arrows indicate the sites with which the quinone-based compound interacts. Gray, white, yellow, red, and blue spheres represent carbon, hydrogen, sulfur, oxygen, and nitrogen atoms, respectively. (e) ΔE_{ads} at 300 K of each quinone on HEDGE surface calculated by DFT.

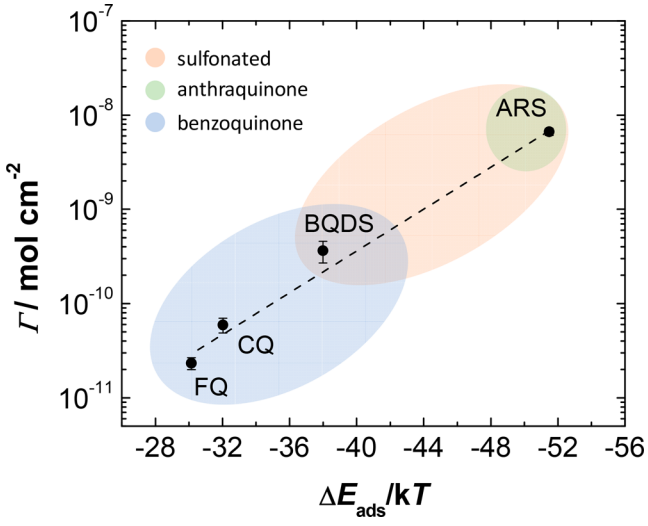

Figure 6. Surface excess vs calculated $\Delta E_{ads}/kT$ (T = 300 K) for each quinone on the HEDGE.

from the 9,10-quinone functionality. As observed for HEDGE, the molecule−surface distances (2.8−3.7 Å) are corresponding to the van der Waals force range, which suggest physisorption of the molecules on HEDGE-nO. The values of ΔE_{ads} of the quinone derivatives on HEDGE-nO were calculated to be −16.22, −17.43, −34.26, and −29.83 kcal mol^{-1}, for FQ, CQ, BQDS, and ARS, respectively.

Comparing the calculated ΔE_{ads} values on HEDGE and HEDGE-nO, it is observed that the presence of oxygen-containing functional groups on the surface differentially affects its interaction with some quinone derivatives. Notably, ΔE_{ads} of BQDS is higher on HEDGE-nO than HEDGE, whereas the ΔE_{ads} of the other molecules are slightly lower on HEDGE-nO, as expected, given oxygenated functional groups present on HEDGE surface can contribute to slightly stronger attraction through dipole−dipole or dipole−induced dipole interactions. In addition, a deviation from the correlation between the experimental values of surface excess and ΔE_{ads} per molecule entity on HEDGE-nO is obtained (Figure S12). The calculated ΔE_{ads} per BQDS molecule on HEDGE-nO is higher than that calculated for ARS; however, the quantity of adsorbed BQDS on the electrode obtained by electrochemical measurements is lower than ARS. This deviation means the presence of oxygenated functional groups on the electrode surface significantly influences the experimental results of surface excess. In summary, the agreement of the calculated

https://dx.doi.org/10.1021/acsaem.9b02357
ACS Appl. Energy Mater. 2020, 3, 1933−1943

ΔE_{ads} with experimental adsorption results implies that the oxygen functional groups, C═O and C−O, on a HEDGE surface play an important role in the interaction with quinone derivatives.

3. CONCLUSIONS

Electron transfer kinetics of the different quinone derivatives is strongly affected by the structure of carbon-based electrode. The electrochemical reversibility of all studied quinone-based molecules was improved by using a HEDGE, which presents oxygenated functional groups, such as C−O and C═O, and a higher density of edge-like defects compared to GC and HOPG. The electron transfer kinetics is controlled by species adsorbed onto HEDGE. The quantity of adsorbed molecules varies among the quinone derivatives by more than 2 orders of magnitude, with surface excess ascending in the order FQ < CQ < BQDS < ARS. Quantum mechanics with molecular dynamics provided atomistic insight into the quinone adsorption. The lowest energy configurations showed molecules interact with HEDGE surfaces by three or four points, with interatomic distances from 2.77 to 4.73 Å, and total ΔE_{ads} of −17.98, −19.10, −22.65, and −30.69 kcal mol^{-1} for FQ, CQ, BQDS, and ARS, respectively, revealing a physisorption process. Adsorption appears to be driven by interactions between C═O and C−O functional groups on the HEDGE surface and the functional groups of quinone-based molecules. The presence of sulfonic acid side groups and the greater number of aromatic rings in the molecular structure may contribute to a higher stabilization of quinone derivatives on HEDGE, which is suggested by ΔE_{ads} and surface excess values. Therefore, this study provides a first glimpse into how carbon-based surfaces with edge-like defects and oxygenated functional groups lead to fast electron transfer kinetics and the adsorption of quinone derivatives. We suggest that this study can guide the development of high-performance carbon-based electrodes for organic electrochemical devices.

■ ASSOCIATED CONTENT

Supporting Information

The Supporting Information is available free of charge at https://pubs.acs.org/doi/10.1021/acsaem.9b02357.

Synthesis and characterization of the FQ and CQ; detailed experimental procedures and computational calculations (PDF)

■ AUTHOR INFORMATION

Corresponding Authors

Frank N. Crespilho − *São Carlos Institute of Chemistry, University of São Paulo (USP), São Carlos, São Paulo 13560-970, Brazil; Harvard John A. Paulson School of Engineering and Applied Sciences, Cambridge, Massachusetts 02138, United States;* orcid.org/0000-0003-4830-652X; Email: frankcrespilho@iqsc.usp.br

Michael J. Aziz − *Harvard John A. Paulson School of Engineering and Applied Sciences, Cambridge, Massachusetts 02138, United States;* orcid.org/0000-0001-9657-9456; Email: maziz@harvard.edu

Authors

Graziela C. Sedenho − *São Carlos Institute of Chemistry, University of São Paulo (USP), São Carlos, São Paulo 13560-970, Brazil; Harvard John A. Paulson School of Engineering and Applied Sciences, Cambridge, Massachusetts 02138, United States;* orcid.org/0000-0001-8696-5978

Diana De Porcellinis − *Harvard John A. Paulson School of Engineering and Applied Sciences, Cambridge, Massachusetts 02138, United States*

Yan Jing − *Department of Chemistry and Chemical Biology, Harvard University, Cambridge, Massachusetts 02138, United States;* orcid.org/0000-0002-5669-4609

Emily Kerr − *Department of Chemistry and Chemical Biology, Harvard University, Cambridge, Massachusetts 02138, United States*

Luis Martin Mejia-Mendoza − *Department of Chemistry and Chemical Biology, Harvard University, Cambridge, Massachusetts 02138, United States*

Álvaro Vazquez-Mayagoitia − *Argonne Leadership Computing Facility, Argonne National Laboratory, Argonne, Illinois 60439, United States*

Alán Aspuru-Guzik − *Department of Chemistry and Chemical Biology, Harvard University, Cambridge, Massachusetts 02138, United States; Department of Chemistry and Department of Computer Science, University of Toronto, Toronto, Ontario M5S 3H6, Canada;* orcid.org/0000-0002-8277-4434

Roy G. Gordon − *Department of Chemistry and Chemical Biology, Harvard University, Cambridge, Massachusetts 02138, United States;* orcid.org/0000-0001-5980-268X

Complete contact information is available at: https://pubs.acs.org/10.1021/acsaem.9b02357

Notes

The authors declare no competing financial interest.

■ ACKNOWLEDGMENTS

Research at Harvard was supported by U.S. DOE Award DE-AC05-76RL01830 through PNNL Subcontract 428977. G.C.S. and F.N.C. gratefully acknowledge the financial support provided by the FAPESP (Projects 2015/22973-6, 2017/15714-0, and 2013/14262-7) and CNPq (Project 203299/2017-5). L.M.M.-M. thanks the support of FONCICYT under Contracts FONCICYT/51/2017 and FONCICYT/56/2018. A.V.-M. acknowledges the Leadership Computing Facility at Argonne National Laboratory for the computing resources for this work. We thank Dr. Liuchuan Tong for bringing to our attention the reversibility of the high-potential redox transition of ARS when adsorbed. A.A.-G. is thankful to Anders G. Fröseth for his support.

■ REFERENCES

(1) Soloveichik, G. L. Flow Batteries: Current Status and Trends. *Chem. Rev.* **2015**, *115* (20), 11533−11558.

(2) Alotto, P.; Guarnieri, M.; Moro, F. Redox Flow Batteries for the Storage of Renewable Energy: A Review. *Renewable Sustainable Energy Rev.* **2014**, *29*, 325−335.

(3) Barnhart, C. J.; Benson, S. M. On the Importance of Reducing the Energetic and Material Demands of Electrical Energy Storage. *Energy Environ. Sci.* **2013**, *6* (4), 1083−1092.

(4) Milton, R. D.; Hickey, D. P.; Abdellaoui, S.; Lim, K.; Wu, F.; Tan, B.; Minteer, S. D. Rational Design of Quinones for High Power Density Biofuel Cells. *Chem. Sci.* **2015**, *6*, 4867−4875.

(5) Giroud, F.; Milton, R. D.; Tan, B.; Minteer, S. D. Simplifying Enzymatic Biofuel Cells: Immobilized Naphthoquinone as a Biocathodic Orientational Moiety and Bioanodic Electron Mediator. *ACS Catal.* **2015**, *5*, 1240−1244.

(6) Gross, A. J.; Chen, X.; Giroud, F.; Abreu, C.; Le Goff, A.; Holzinger, M.; Cosnier, S. A High Power Buckypaper Biofuel Cell:

Exploiting 1,10- Phenanthroline-5,6-Dione with FAD-Dependent Dehydrogenase for Catalytically-Powerful Glucose Oxidation. *ACS Catal.* **2017**, *7*, 4408−4416.
(7) Gerhardt, M. R.; Tong, L.; Gómez-Bombarelli, R.; Chen, Q.; Marshak, M. P.; Galvin, C. J.; Aspuru-Guzik, A.; Gordon, R. G.; Aziz, M. J. Anthraquinone Derivatives in Aqueous Flow Batteries. *Adv. Energy Mater.* **2017**, *7* (8), 1601488.
(8) Yang, Z.; Tong, L.; Tabor, D. P.; Beh, E. S.; Goulet, M. A.; De Porcellinis, D.; Aspuru-Guzik, A.; Gordon, R. G.; Aziz, M. J. Alkaline Benzoquinone Aqueous Flow Battery for Large-Scale Storage of Electrical Energy. *Adv. Energy Mater.* **2018**, *8* (8), 1−9.
(9) Lin, K.; Chen, Q.; Gerhardt, M. R.; Tong, L.; Kim, S. B.; Eisenach, L.; Valle, A. W.; Hardee, D.; Gordon, R. G.; Aziz, M. J.; Marshak, M. P. Alkaline Quinone Flow Battery. *Science* **2015**, *349* (6255), 1529−1532.
(10) Huskinson, B.; Marshak, M. P.; Suh, C.; Er, S.; Gerhardt, M. R.; Galvin, C. J.; Chen, X.; Aspuru-Guzik, A.; Gordon, R. G.; Aziz, M. J. A Metal-Free Organic-Inorganic Aqueous Flow Battery. *Nature* **2014**, *505* (7482), 195−198.
(11) Bailey, S. I.; Ritchie, I. M. A Cyclic Voltammetric Study of the Aqueous Electrochemistry of Some Quinones. *Electrochim. Acta* **1985**, *30* (1), 3−12.
(12) Song, Y.; Buettner, G. R. Thermodynamic and Kinetic Considerations for the Reaction of Semiquinone Radicals to Form Superoxide and Hydrogen Peroxide. *Free Radical Biol. Med.* **2010**, *49* (6), 919−962.
(13) Winsberg, J.; Hagemann, T.; Janoschka, T.; Hager, M. D.; Schubert, U. S. Redox-Flow Batteries: From Metals to Organic Redox-Active Materials. *Angew. Chem., Int. Ed.* **2017**, *56* (3), 686−711.
(14) Suresh, S.; Ulaganathan, M.; Aswathy, R.; Ragupathy, P. Enhancement of Bromine Reversibility Using Chemically Modified Electrodes and Their Applications in Zinc Bromine Hybrid Redox Flow Battery. *ChemElectroChem* **2018**, *5*, 3411−3418.
(15) Chen, Q.; Gerhardt, M. R.; Hartle, L.; Aziz, M. J. A Quinone-Bromide Flow Battery with 1 W/Cm2 Power Density. *J. Electrochem. Soc.* **2016**, *163* (1), A5010−A5013.
(16) Yang, B.; Hoober-Burkhardt, L.; Wang, F.; Surya Prakash, G. K.; Narayanan, S. R. An Inexpensive Aqueous Flow Battery for Large-Scale Electrical Energy Storage Based on Water-Soluble Organic Redox Couples. *J. Electrochem. Soc.* **2014**, *161* (9), A1371−A1380.
(17) Lin, K.; Gómez-Bombarelli, R.; Beh, E. S.; Tong, L.; Chen, Q.; Valle, A.; Aspuru-Guzik, A.; Aziz, M. J.; Gordon, R. G. A Redox-Flow Battery with an Alloxazine-Based Organic Electrolyte. *Nat. Energy* **2016**, *1* (9), 1−8.
(18) Kwabi, D. G.; Lin, K.; Ji, Y.; Kerr, E. F.; Goulet, M.-A.; De Porcellinis, D.; Tabor, D. P.; Pollack, D. A.; Aspuru-Guzik, A.; Gordon, R. G.; Aziz, M. J. Alkaline Quinone Flow Battery with Long Lifetime at pH 12. *Joule* **2018**, *2*, 1894−1906.
(19) Pezeshki, A. M.; Clement, J. T.; Veith, G. M.; Zawodzinski, T. A.; Mench, M. M. High Performance Electrodes in Vanadium Redox Flow Batteries through Oxygen-Enriched Thermal Activation. *J. Power Sources* **2015**, *294*, 333−338.
(20) He, Z.; Jiang, Y.; Li, Y.; Zhu, J.; Zhou, H.; Meng, W.; Wang, L.; Dai, L. Carbon Layer-Exfoliated, Wettability-Enhanced, SO3H-Functionalized Carbon Paper: A Superior Positive Electrode for Vanadium Redox Flow Battery. *Carbon* **2018**, *127*, 297−304.
(21) Liu, T.; Wei, X.; Nie, Z.; Sprenkle, V.; Wang, W. A Total Organic Aqueous Redox Flow Battery Employing a Low Cost and Sustainable Methyl Viologen Anolyte and 4-HO-TEMPO Catholyte. *Adv. Energy Mater.* **2016**, *6* (3), 1501449.
(22) Wei, L.; Zhao, T. S.; Zhao, G.; An, L.; Zeng, L. A High-Performance Carbon Nanoparticle-Decorated Graphite Felt Electrode for Vanadium Redox Flow Batteries. *Appl. Energy* **2016**, *176*, 74−79.
(23) Kabtamu, D. M.; Chen, J.-Y.; Chang, Y.-C.; Wang, C.-H. Water-Activated Graphite Felt as a High-Performance Electrode for Vanadium Redox Flow Batteries. *J. Power Sources* **2017**, *341*, 270−279.
(24) González, Z.; Flox, C.; Blanco, C.; Granda, M.; Morante, J. R.; Menéndez, R.; Santamaría, R. Outstanding Electrochemical Performance of a Graphene-Modified Graphite Felt for Vanadium Redox Flow Battery Application. *J. Power Sources* **2017**, *338*, 155−162.
(25) Mustafa, I.; Lopez, I.; Younes, H.; Susantyoko, R. A.; Al-Rub, R. A.; Almheiri, S. Fabrication of Freestanding Sheets of Multiwalled Carbon Nanotubes (Buckypapers) for Vanadium Redox Flow Batteries and Effects of Fabrication Variables on Electrochemical Performance. *Electrochim. Acta* **2017**, *230*, 222−235.
(26) Park, M.; Jeon, I. Y.; Ryu, J.; Baek, J. B.; Cho, J. Exploration of the Effective Location of Surface Oxygen Defects in Graphene-Based Electrocatalysts for All-Vanadium Redox-Flow Batteries. *Adv. Energy Mater.* **2015**, *5* (5), 1−7.
(27) Pour, N.; Kwabi, D. G.; Carney, T.; Darling, R. M.; Perry, M. L.; Shao-Horn, Y. Influence of Edge-and Basal-Plane Sites on the Vanadium Redox Kinetics for Flow Batteries. *J. Phys. Chem. C* **2015**, *119* (10), 5311−5318.
(28) Taylor, S. M.; Pătru, A.; Perego, D.; Fabbri, E.; Schmidt, T. J. Influence of Carbon Material Properties on Activity and Stability of the Negative Electrode in Vanadium Redox Flow Batteries: A Model Electrode Study. *ACS Appl. Energy Mater.* **2018**, *1*, 1166−1174.
(29) Park, M.; Beh, E. S.; Fell, E. M.; Jing, Y.; Kerr, E. F.; Porcellinis, D.; Goulet, M.-A.; Ryu, J.; Wong, A. A.; Gordon, R. G.; Cho, J.; Aziz, M. J. A High-Voltage Aqueous Zinc-Organic Hybrid Flow Battery. *Adv. Energy Mater.* **2019**, *9*, 1900694.
(30) Imai, K.; Nakanishi, I.; Ohno, A.; Kurihara, M.; Miyata, N.; Matsumoto, K. I.; Nakamura, A.; Fukuhara, K. Synthesis and Radical-Scavenging Activity of a Dimethyl Catechin Analogue. *Bioorg. Med. Chem. Lett.* **2014**, *24* (11), 2582−2584.
(31) Er, S.; Suh, C.; Marshak, M. P.; Aspuru-Guzik, A. Computational Design of Molecules for an All-Quinone Redox Flow Battery. *Chem. Sci.* **2015**, *6* (2), 885−893.
(32) Carretero-González, J.; Castillo-Martínez, E.; Armand, M. Highly Water-Soluble Three-Redox State Organic Dyes as Bifunctional Analytes. *Energy Environ. Sci.* **2016**, *9* (11), 3521−3530.
(33) Tong, L.; Jing, Y.; Gordon, R. G.; Aziz, M. J. Symmetric All-Quinone Aqueous Battery. *ACS Appl. Energy Mater.* **2019**, *2*, 4016−4021.
(34) Kabir, H.; Gyan, I. O.; Francis Cheng, I. Electrochemical Modification of a Pyrolytic Graphite Sheet for Improved Negative Electrode Performance in the Vanadium Redox Flow Battery. *J. Power Sources* **2017**, *342*, 31−37.
(35) Zhong, J. H.; Zhang, J.; Jin, X.; Liu, J. Y.; Li, Q.; Li, M. H.; Cai, W.; Wu, D. Y.; Zhan, D.; Ren, B. Quantitative Correlation between Defect Density and Heterogeneous Electron Transfer Rate of Single Layer Graphene. *J. Am. Chem. Soc.* **2014**, *136* (47), 16609−16617.
(36) Yuan, W.; Zhou, Y.; Li, Y.; Li, C.; Peng, H.; Zhang, J.; Liu, Z.; Dai, L.; Shi, G. The Edge- and Basal-Plane-Specific Electrochemistry of a Single-Layer Graphene Sheet. *Sci. Rep.* **2013**, *3* (Cvd), 1−7.
(37) Moore, R. R.; Banks, C. E.; Compton, R. G. Basal Plane Pyrolytic Graphite Modified Electrodes: Comparison of Carbon Nanotubes and Graphite Powder as Electrocatalysts. *Anal. Chem.* **2004**, *76* (10), 2677−2682.
(38) Tao, L.; Wang, Q.; Dou, S.; Ma, Z.; Huo, J.; Wang, S.; Dai, L. Edge-Rich and Dopant-Free Graphene as a Highly Efficient Metal-Free Electrocatalyst for the Oxygen Reduction Reaction. *Chem. Commun.* **2016**, *52* (13), 2764−2767.
(39) Beh, E. S.; De Porcellinis, D.; Gracia, R. L.; Xia, K. T.; Gordon, R. G.; Aziz, M. J. A Neutral PH Aqueous Organic-Organometallic Redox Flow Battery with Extremely High Capacity Retention. *ACS Energy Lett.* **2017**, *2* (3), 639−644.
(40) Harris, P. J. F. Fullerene-Related Structure of Commercial Glassy Carbons. *Philos. Mag.* **2004**, *84* (29), 3159−3167.
(41) Bukalov, S. S.; Zubavichus, Y. V.; Leites, L. A.; Sorokin, A. I.; Kotosonov, A. S. Structural Changes in Industrial Glassy Carbon As a Function of Heat Treatment Temperature According To Raman Spectroscopy and X-Ray. *Nanosyst. Phys., Chem. Math.* **2014**, *5* (1), 186−191.

https://dx.doi.org/10.1021/acsaem.9b02357
ACS Appl. Energy Mater. 2020, 3, 1933−1943

(42) Banks, C. E.; Davies, T. J.; Wildgoose, G. G.; Compton, R. G. Electrocatalysis at Graphite and Carbon Nanotube Modified Electrodes: Edge-Plane Sites and Tube Ends Are the Reactive Sites. *Chem. Commun.* **2005**, No. 7, 829−841.
(43) Macedo, L. J. A.; Lima, F. C. D. A.; Amorim, R. G.; Freitas, R. O.; Yadav, A.; Iost, R. M.; Balasubramanian, K.; Crespilho, F. N. Interplay of Non-Uniform Charge Distribution on the Electrochemical Modification of Graphene. *Nanoscale* **2018**, *10*, 15048−15057.
(44) McCreery, R. L. Advanced Carbon Electrode Materials for Molecular Electrochemistry. *Chem. Rev.* **2008**, *108* (7), 2646−2687.
(45) Sites, E. P.; Neumann, C. C. M.; Batchelor-McAuley, C.; Downing, C.; Compton, R. G. Anthraquinone Monosulfonate Adsorbed on Graphite Shows Two Very Different Rates of Electron Transfer: Surface Heterogeneity Due to Basal. *Chem. - Eur. J.* **2011**, *17*, 7320−7326.
(46) Maldonado, S.; Morin, S.; Stevenson, K. J. Electrochemical Oxidation of Catecholamines and Catechols at Carbon Nanotube Electrodes. *Analyst* **2006**, *131*, 262−267.
(47) Dai, H. P.; Shiu, K. K. Voltammetric Behavior of Alizarin Red S Adsorbed on Electrochemically Pretreated Glassy Carbon Electrodes. *Electrochim. Acta* **1998**, *43* (18), 2709−2715.
(48) Schumacher, S.; Nagel, T.; Scheller, F. W.; Gajovic-Eichelmann, N. Alizarin Red S as an Electrochemical Indicator for Saccharide Recognition. *Electrochim. Acta* **2011**, *56* (19), 6607−6611.
(49) Pimenta, M. A.; Dresselhaus, G.; Dresselhaus, M. S.; Cançado, L. G.; Jorio, A.; Saito, R. Studying Disorder in Graphite-Based Systems by Raman Spectroscopy. *Phys. Chem. Chem. Phys.* **2007**, *9* (11), 1276−1290.
(50) Ferrari, A. C.; Robertson, J. Interpretation of Raman Spectra of Disordered and Amorphous Carbon. *Phys. Rev. B: Condens. Matter Mater. Phys.* **2000**, *61* (20), 14095−14107.
(51) Kozlowski, C.; Sherwood, P. M. A. X-Ray Photoelectron-Spectroscopic Studies of Carbon-Fibre Surfaces. *J. Chem. Soc., Faraday Trans. 1* **1985**, *81*, 2745−2756.
(52) Zhao, L.; Wu, G.; Cai, Z.; Zhao, T.; Yao, Q.; Chen, X. Ultrasensitive Non-Enzymatic Glucose Sensing at near-Neutral PH Values via Anodic Stripping Voltammetry Using a Glassy Carbon Electrode Modified with Pt3Pd Nanoparticles and Reduced Graphene Oxide. *Microchim. Acta* **2015**, *182* (11−12), 2055−2060.
(53) Mejía-Mendoza, L. M.; Valdez-Gonzalez, M.; Muñiz, J.; Santiago, U.; Cuentas-Gallegos, A. K.; Robles, M. A Theoretical Approach to the Nanoporous Phase Diagram of Carbon. *Carbon* **2017**, *120*, 233−243.
(54) Deringer, V. L.; Merlet, C.; Hu, Y.; Lee, T. H.; Kattirtzi, J. A.; Pecher, O.; Csányi, G.; Elliott, S. R.; Grey, C. P. Towards an Atomistic Understanding of Disordered Carbon Electrode Materials. *Chem. Commun.* **2018**, *54* (47), 5988−5991.
(55) Ortmann, F.; Schmidt, W. G.; Bechstedt, F. Attracted by Long-Range Electron Correlation: Adenine on Graphite. *Phys. Rev. Lett.* **2005**, *95*, 186101.
(56) Ashino, M.; Schwarz, A.; Behnke, T.; Wiesendanger, R. Atomic-Resolution Dynamic Force Microscopy and Spectroscopy of a Single-Walled Carbon Nanotube: Characterization of Interatomic van Der Waals Forces. *Phys. Rev. Lett.* **2004**, *93*, 136101.
(57) Allen, F. H.; Watson, D. G.; Brammer, L.; Orpen, A. G.; Taylor, R. Typical Interatomic Distances: Organic Compounds. *Int. Tables Crystallogr.* **2006**, *C*, 790−811.

https://dx.doi.org/10.1021/acsaem.9b02357
ACS Appl. Energy Mater. 2020, 3, 1933−1943

SUPPORTING INFORMATION

Effect of molecular structure of quinones and carbon electrode surfaces on the interfacial electron transfer process

Graziela C. Sedenho[1,2], Diana De Porcellinis[2], Yan Jing[3], Emily Kerr[3], Luis Martin Mejia-Mendoza[3], Álvaro Vázquez-Mayagoitia[4], Alán Aspuru-Guzik[3,5], Roy G. Gordon[2,3], Frank N. Crespilho[1,2]*, Michael J. Aziz[2]*

[1] *São Carlos Institute of Chemistry, University of São Paulo (USP), São Carlos, São Paulo 13560-970, Brazil.*

[2] *Harvard John A. Paulson School of Engineering and Applied Sciences, Cambridge, Massachusetts 02138, USA.*

[3] *Department of Chemistry and Chemical Biology, Harvard University, Cambridge, Massachusetts 02138, USA.*

[4] *Argonne Leadership Computing Facility, Argonne National Laboratory, Argonne, Illinois 60439, USA.*

[5] *Department of Chemistry, Department of Computer Science, University of Toronto,Toronto, Ontario M5S 3H6, Canada.*

*Corresponding authors:

Michael J. Aziz
E-mail: maziz@harvard.edu

Frank N. Crespilho
E-mail: frankcrespilho@iqsc.usp.br

Table of Contents

1. FQH_2 synthesis and characterization. 10 grams of 1,4-hydroquinone (90.8 mmol) was added to a 1 L round bottom flask with 134 mL of 37 wt% formaldehyde solution (1801 mmol) and 272 ml of 40 weight percent dimethyl amine in water (2148 mmol). The reaction was stirred at reflux for 5 hours and then vacuum filtered. The product was analyzed by ^{1}H NMR without further purification (yield: 51.2%).[1]

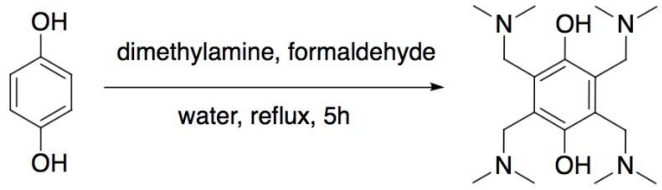

Scheme S1 Synthesis of FQH_2.

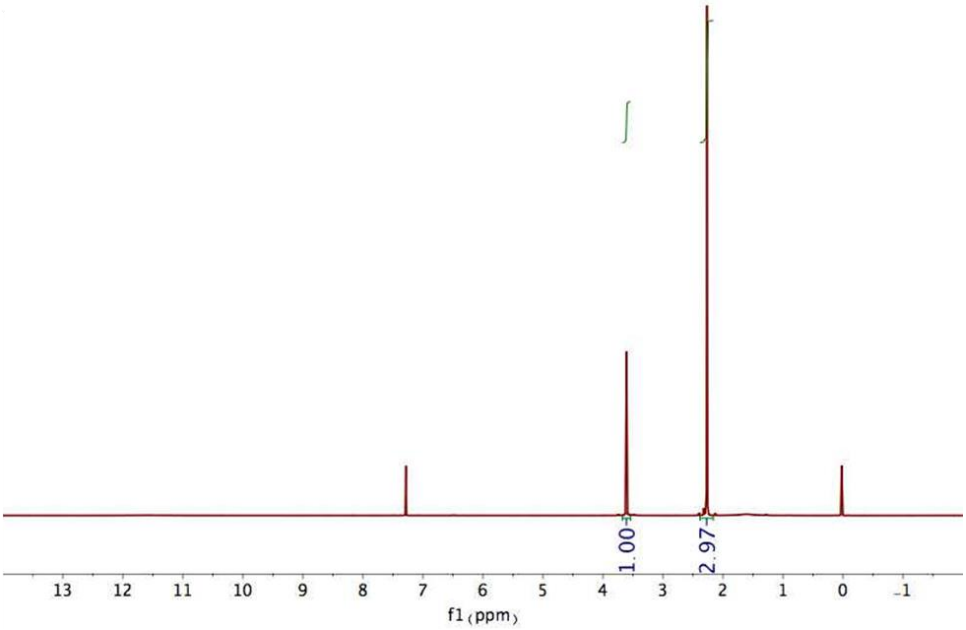

Figure S1. ^{1}H NMR spectrum of FQH_2. ^{1}H NMR (500 MHz, $CDCl_3$): δ 3.63 (s, 8H), 2.27 (s, 24H).

2. CQH_2 synthesis and characterization. A mixture of formaldehyde 37 wt% water solution (16.2 g, 0.2 mol) and morpholine (17.4 g, 0.2 mol) in isopropanol (70 mL) was added to a 250 mL

round-bottom Schlenk flask, under nitrogen protection. Catechol (11.0 g, 0.1 mol) was added and the solution was refluxed for overnight. After that, the solution was cooled down to room temperature and filtered, and washed by ethanol to give the final product (21.6 g, yield: 70%). Figure S2 shows ^{1}H NMR of the obtained product. The chemical shifts are same as the values previously reported for CQH_2.[2]

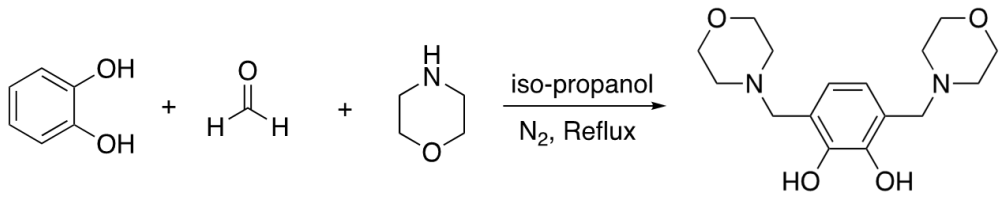

Scheme S2 Synthesis of CQH_2.

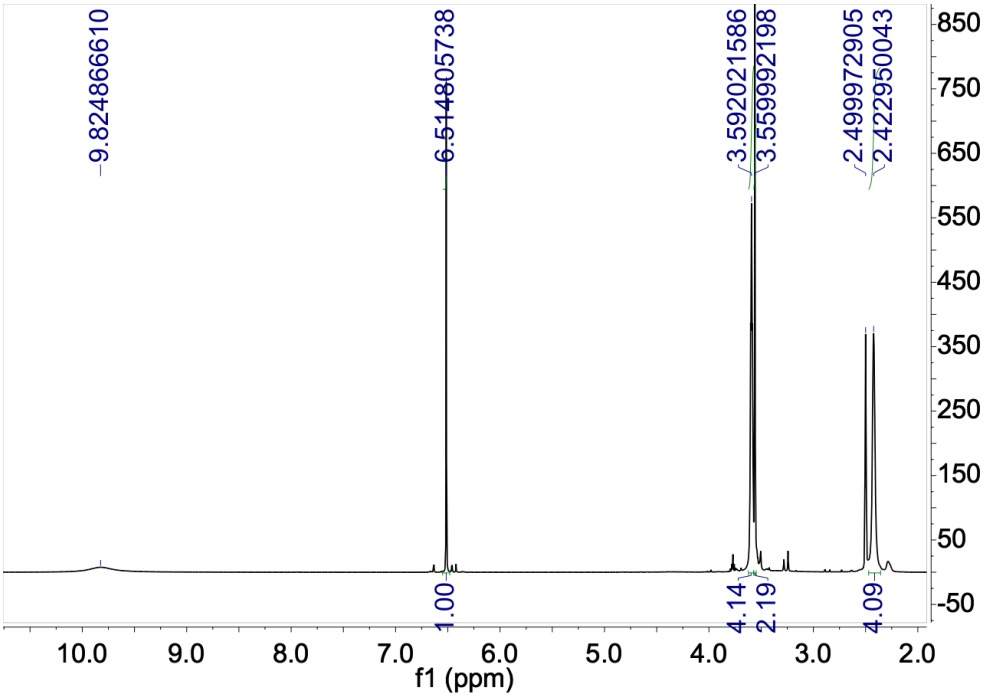

Figure S2. ^{1}H NMR of CQH_2 in DMSO-d6.

3. Electrochemical measurements. All electrochemical measurements were conducted on a Gamry Reference 3000 potentiostat (Gamry Instruments, United States) using Pt wire and Ag/AgCl electrode (3 mol L^{-1} NaCl filling solution) as counter and reference electrodes,

respectively. Both electrodes were obtained from BASi® (United States). The potential of the Ag/AgCl reference electrode is +0.213 V versus the standard hydrogen electrode (SHE). Glassy carbon electrode (from BASi®, United States) with area of 0.071 cm^2, highly ordered pyrolytic graphite (HOPG) plate (from SPI Supplies Division of Structure Probe, Inc., United States) and high edge-density graphite electrode (HEDGE) were used as working electrodes. Before the experiments, glassy carbon electrode was cleaned by polishing in 0.3 μm and 0.05 μm alumina slurry, followed by sonication in deionized water for 5 minutes. HEDGE was freshly prepared before the electrochemical experiments. HEDGE was prepared by manually polishing a graphite rod with diameter of 6.1 mm on abrasive sheet 413Q 240 (3M™ Wetordry™, United States) at an inclination of approximately 45°. After the polishing, the electrode surface was washed with deionized water to remove the unattached particles. This polishing process exposes the edge planes of the graphitic structure, obtaining an electrode with higher density of exposed edge planes compared to the pristine graphite. HOPG was cleaned before the measurements by the scotch tape method. The tape was pressed onto the HOPG surface and then pulled off taking the top layers of the HOPG. The area of HEDGE and HOPG electrodes were delimited by nitrocellulose resin, in order to expose only the polished face with edge planes and the basal-plane surface, respectively to the electrolyte (see Figure S3). The exposed areas of HEDGE and HOPG were 0.559 ± 0.017 cm^2 and 0.291 cm^2, respectively.

All electrochemical measurements were performed at room temperature in degassed 1.0 mol L^{-1} H_2SO_4 solution as supporting electrolyte. Sulfuric acid (H_2SO_4; 96%) was purchased from KMG Electronic Chemical, Inc. (United States), and the commercial quinones BQDS disodium salt monohydrate (97%) and ARS sodium salt were obtained from Alfa Aesar (United States) and Sigma-Aldrich (United States), respectively.

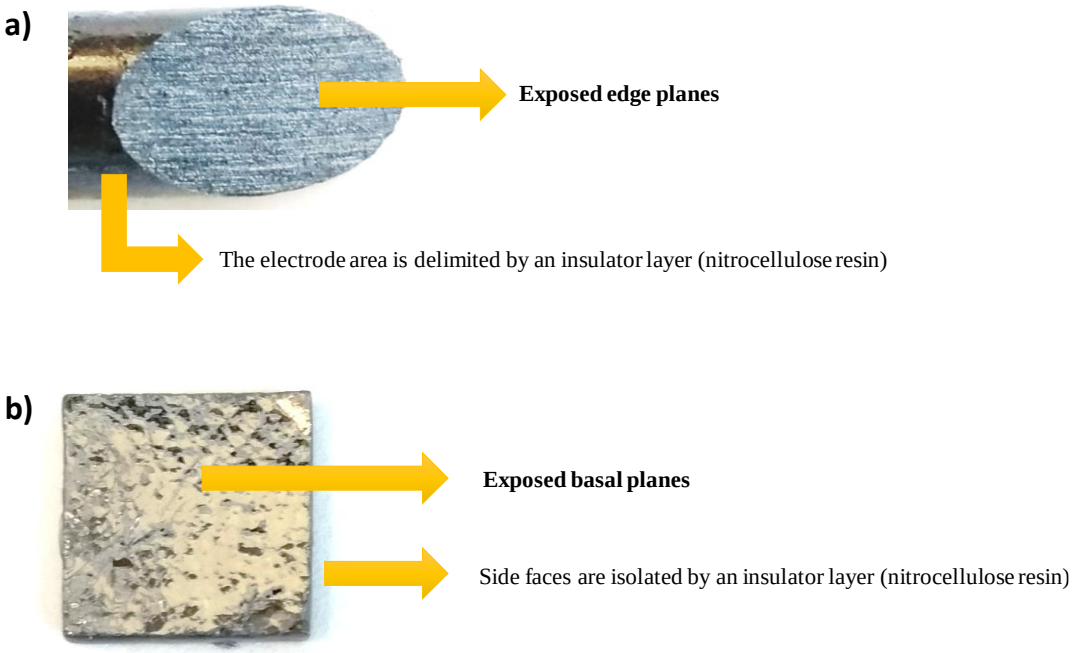

Figure S3. (a) HEDGE (geometric area = 0.559 ± 0.017 cm^2) and (b) HOPG (geometric area = 0.291 cm^2) electrodes. The area of both electrodes was delimited by nitrocellulose resin, exposing only the edge plane or basal plane faces.

4. Diagnosis of electrochemical reversibility. To investigate the electrochemical reversibility of redox reactions by cyclic voltammetry, the difference between the anodic and cathodic peak potentials, or peak-to-peak separation (ΔE_p) was used. Assuming ideal Nernstian behavior, the equilibrium electrode potential obeys the Nernst equation, and we ignore the influence of electron transfer kinetics at the electrode/electrolyte interface. For a reversible system involving freely diffusing redox species, ΔE_p is given by Equation S1:

$$\Delta E_p = 2.22RT/nF \quad \text{(Equation S1)}$$

where, R is the gas constant, T is the absolute temperature, n is the number of electrons involved in the reaction, and F is the Faraday constant.[3] According to that, ΔE_p for a reversible two-electron redox reaction is approximately 30 mV at 25 °C. Higher values suggest a quasi-reversible or irreversible electron transfer reaction, whereas smaller values of ΔE_p indicate electron transfer may occur by surface-adsorbed species.[3]

5. Dependence of peak current density on scan rate.

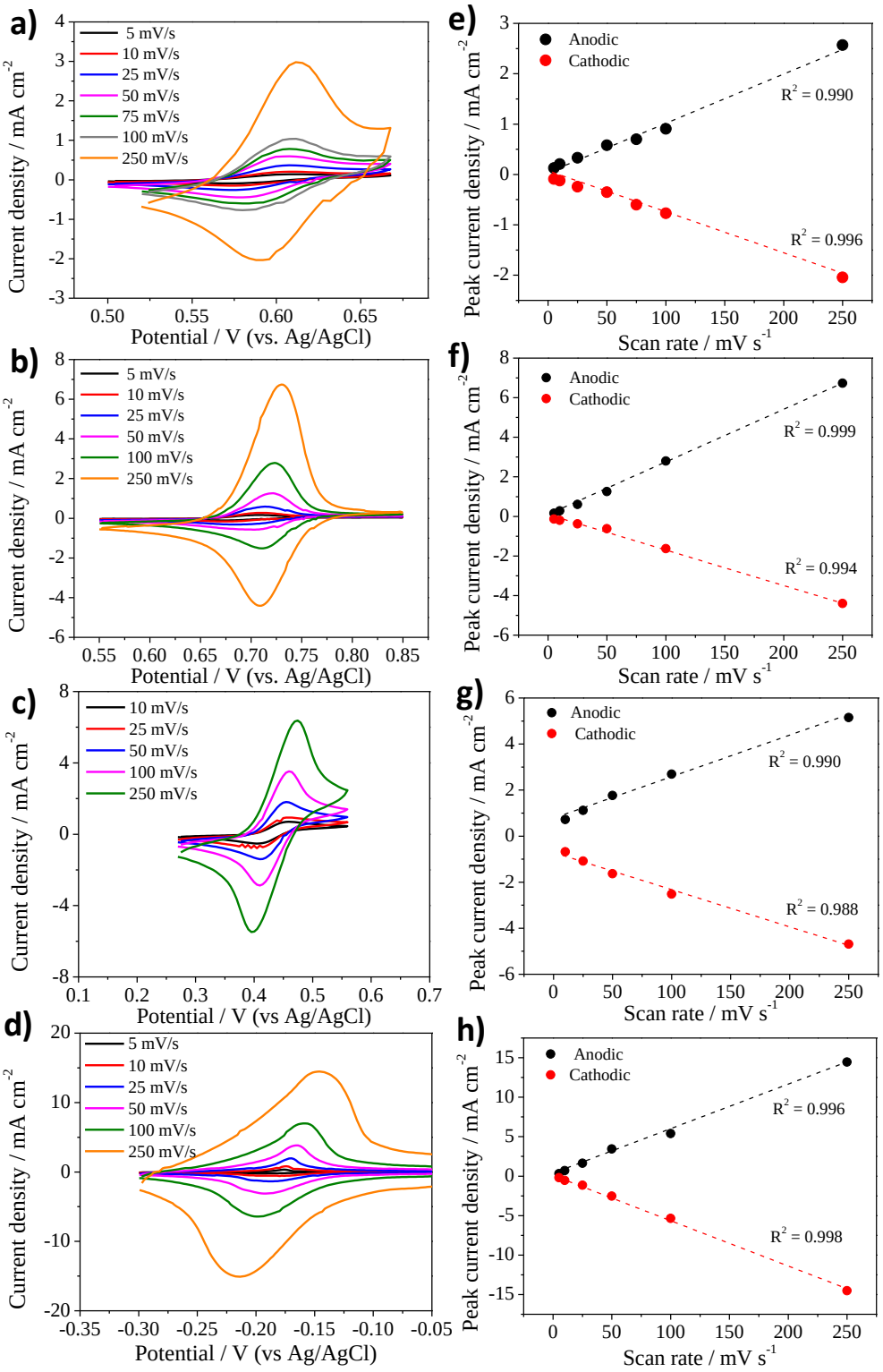

Figure S4. CVs (third cycle) of HEDGE in 1.0 mol L^{-1} H_2SO_4 containing (a) 1.0 mmol L^{-1} CQ, (b) 1.0 mmol L^{-1} BQDS, (c) 10.0 mmol L^{-1} FQ, and (d) 1.0 mmol L^{-1} ARS at different scan rates. Dependence of peak current density on scan rate for (e) CQ, (f) BQDS, (g) FQ and (h) ARS.

6. Scanning electron microscopic measurements. The morphology of HEDGE and HOPG electrodes was investigated by Scanning Electron Microscopes (Zeiss Ultra55). The field emitted is 10 kV, which gives a resolution of around 10 µm.

7. Raman spectroscopic measurements. A Horiba Multiline Raman Spectrometer (model LabRam Evolution) with a 50× lens was used to investigate the near-to-surface structure of the HOPG, HEDGE and GC. The measurements were carried out with a 633 nm excitation laser, grating of 600 line/mm and a laser power of 20 mW. First order Raman spectra were recorded in the range 1000−2000 cm^{-1}. After data acquisition, the baselines of Raman spectra were corrected, and Lorentzian function was used to fit the peaks. Each spectrum was then normalized by the intensity of the highest peaks in order to enable the spectra comparison.

Raman spectrum of GC in Figure S5 shows broad *D* and *G*-bands centered at 1330 cm^{-1} and 1604 cm^{-1}. The intensity ratio, I_D/I_G >1 indicates nano-sized disordered sp^2 carbon.[4]

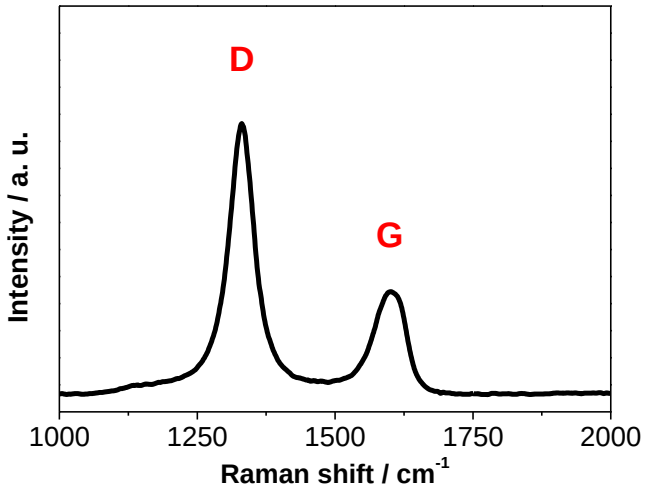

Figure S5. Raman spectrum of GC obtained with 633 nm excitation laser.

8. XPS measurements. For identifying the surface chemistry of the carbon electrodes, a Thermo Scientific K-Alpha X-ray photoelectron spectrometer was used. A monochromatic Al Kα X-ray (hν = 1486.6 eV) radiation was used as excitation source. The operating pressure in the ultra-high

vacuum chamber during the analyses was 8×10^{-8} mbar. The XPS survey spectra were recorded at pass energy of 200.0 eV with a 1.00 eV per step. The high-resolution spectra were recorded at pass energy of 50.0 eV with a 0.100 eV per step. In all measurements the spot size was 40 µm. Curve fitting of the high-resolution XPS spectra was performed following a Shirley-type background subtraction and the spectra were deconvoluted using Voigtian type functions, with combinations of Gaussian (70%) and Lorentzian (30%).

Figure S6 shows the high-resolution XPS spectrum of HEDGE in C 1s region. The spectrum was deconvoluted in four peaks, which can be assigned to: i) C=C (284.5 eV); ii) C–C or C–H (285.1 eV); iii) C=O (aromatic), C–O–H and/or C–O–C (287.0 eV); and iv) π- π* shake-up (290.5 eV), according to literature.[5] On basis of the area of deconvoluted peaks, the percentage of each carbon peak was found: 69.3 % for C=C; 21.6 % for C–C or C–H; 3.6 % for C=O (aromatic), C–O–H and/or C–O–C; and 5.5 % for π- π* shake-up.

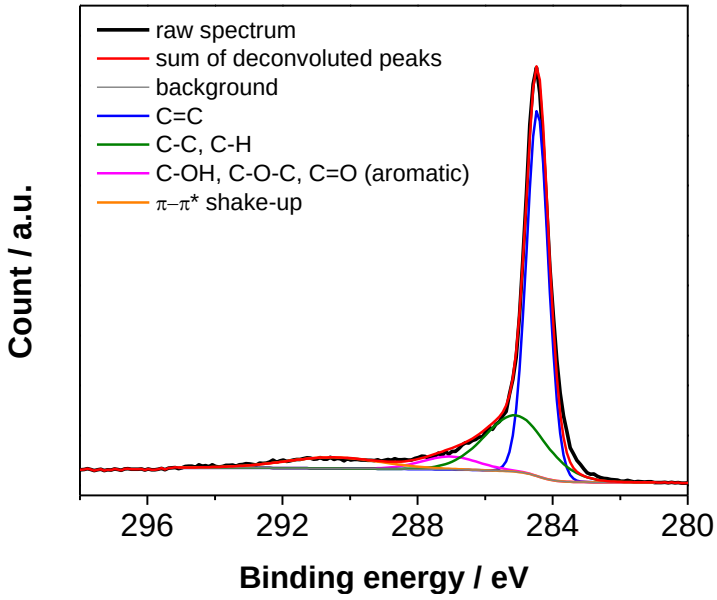

Figure S6. High-resolution spectrum of HEDGE in C 1s region.

9. ECSA of HOPG and HEDGE. The ECSA of the carbon electrodes were investigated by analysis of the double-layer capacitance, based on the method described in the literature.[6] For this,

we recorded CVs in 1.0 mol L^{-1} H_2SO_4 supporting electrolyte at various scan rates from 5 to 100 mV s^{-1} in the non-faradic potential region of 0.20 V to 0.30 V as displayed in the Figures S7a and S7b. Usually, the qualitatively larger CV indicates the higher electrical double layer capacitance (C_{dl}) of the electrode and it is a reliable indicator of higher ECSA. The C_{dl} of the electrodes was calculated by plotting the difference between the anodic (j_a) and cathodic (j_c) capacitive current densities ($\Delta j = j_a - j_c$) at 0.25 V (vs Ag/AgCl) against the scan rates (see Figures S7c and S7d). The slope of this plot was divided by 2 to obtain double layer capacitance of the electrode, according to the Equation S2.

$$C_{\mathrm{dl}} = \frac{1}{2}\frac{\partial(j_a - j_c)}{\partial(scan\ rate)} \quad \text{(Equation S2)}$$

Thus, C_{dl} of HOPG and HEDGE were calculated to be 5.31 µF cm^{-2} and 169.55×10^{-5} µF cm^{-2}, respectively.

For the estimation of ECSA, a specific capacitance (C_s) value of 4.3 µF cm^{-2} was adopted because this is the typical C_s for a flat graphite surface.[7] Thus, the ECSAs can be calculated according to the following Equation S3.

$$\mathrm{ECSA} = \frac{C_{\mathrm{dl}}}{C_{\mathrm{s}}} \quad \text{(Equation S3)}$$

The ECSAs of HOPG and HEDGE were 1.24 cm^2 and 35.53 cm^2, respectively.

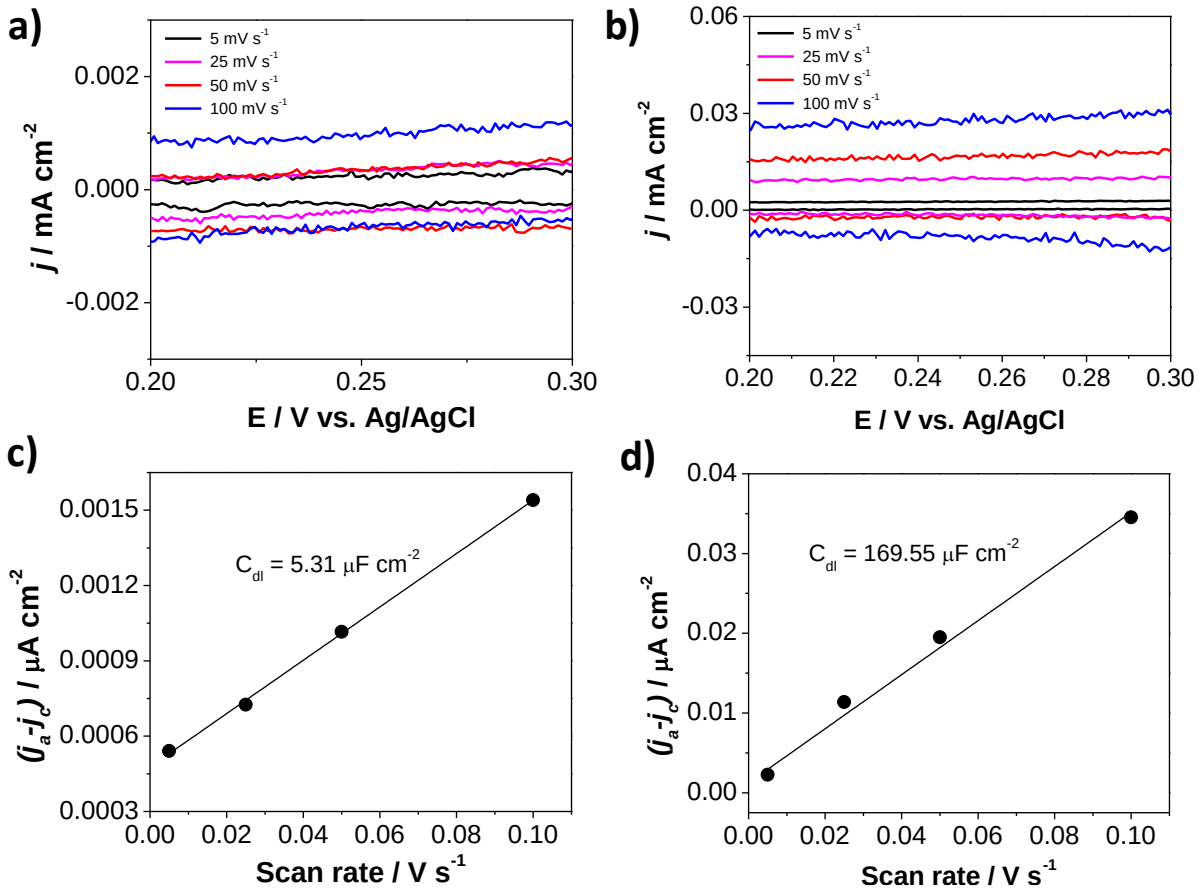

Figure S7. CVs of HOPG (a) and HEDGE (b) and difference between the anodic (j_a) and cathodic (j_c) capacitive current densities at 0.25 V of HOPG (c) and HEDGE (d) plotted against scan rates fitted to linear regression enables the estimation of C_{dl}.

10. Adsorption of quinones on HEDGE. The adsorption of quinone derivative compounds onto HEDGE surfaces was investigated by anodic stripping voltammetry.[8] Freshly prepared HEDGE was exposed to a solution of 1.0 mmol L^{-1} of quinone in degassed 1.0 mol L^{-1} H_2SO_4, then a potential of approximately 50 mV more positive than peak oxidation potential of redox species was applied for 120 s (the chronoamperograms are shown in Figure S8). After that, the electrode was dipped into 1.0 mol L^{-1} H_2SO_4 and kept in 1.0 mol L^{-1} H_2SO_4 for 30 s under magnetic stirring of 60 rpm to remove the non-adsorbed species from the electrode surface. Thereafter, the amount of adsorbed species was evaluated by CVs in clean (without redox species) 1.0 mol L^{-1} H_2SO_4. Figure S9 shows the experimental setup. The surface excess (Γ) of each quinone derivative on HEDGE surface was calculated according Equation S4 based on anodic peak charge.

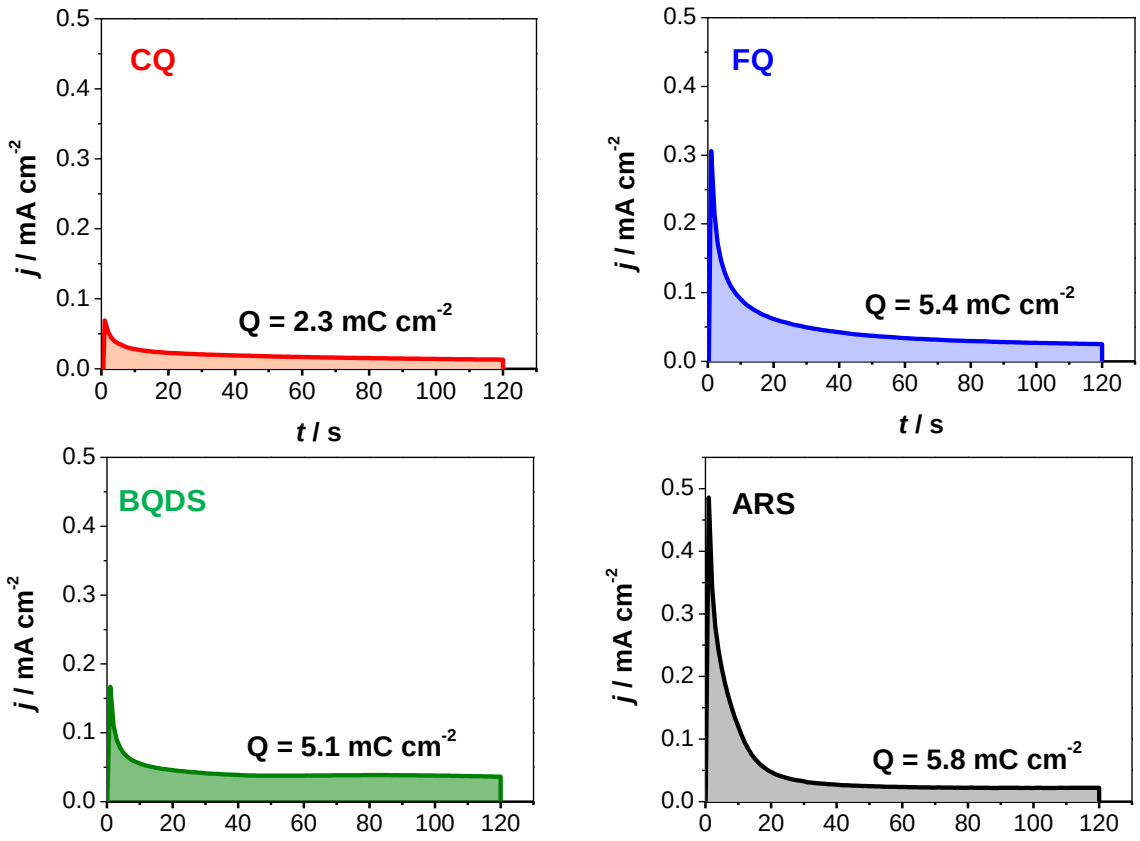

Figure S8. Chronoamperograms of the electro-adsorption in 1.0 mol L^{-1} H_2SO_4 containing 1.0 mmol L^{-1} of each quinone derivative at a potential 50 mV more positive than peak oxidation potential of each species. The backgrounds were previously subtracted.

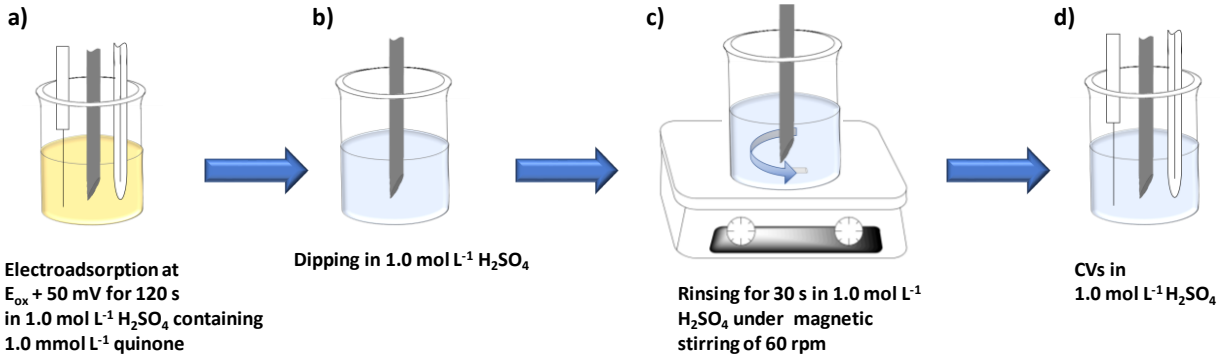

Figure S9. Adsorption quinone experimental setup. (a) Electro-adsorption in degassed 1.0 mol L^{-1} H_2SO_4 containing 1.0 mmol L^{-1} of quinone, for 120 s at a potential approximately 50 mV more positive than peak oxidation potential of the species; (b) electrode dipping in 1.0 mol L^{-1} H_2SO_4; (c) electrode rinsing in 1.0 mol L^{-1} H_2SO_4 for 30 s under magnetic stirring of 60 rpm; and (d) electrochemical measurements in clean electrolyte.

$$\Gamma = \frac{Q}{n\,\mathrm{F}\,A} \quad \text{(Equation S4)}$$

where, Q is the charge of anodic peak (C), n is the number of electrons involved in the reaction (n = 2), F is Faraday constant (96,485 C mol^{-1}) and A is the geometric area of the electrode (cm^2). Q can be calculated by the integration of anodic peak, according Equation S5.

$$Q = \int \frac{j}{\upsilon} dE \quad \text{(Equation S5)}$$

where, j is the faradaic current density, υ is the scan rate (V s^{-1}) and E is the electrical potential. Γ of each quinone was determined to be (2.3 ± 0.3) × 10^{-11} mol cm^{-2}, (5.9 ± 1.0) × 10^{-11} mol cm^{-2}, (3.6 ± 0.9) × 10^{-10} mol cm^{-2} and (6.7 ± 0.6) × 10^{-9} mol cm^{-2} for FQ, CQ, BQDS and ARS, respectively. Assuming the molecules are orientated with their aromatic rings parallel to the electrode surface (as shown in Figure 5a-d), packing with the adsorbed molecules side by side, and the geometric area of the electrodes, it is estimated BQDS and ARS are adsorbed on HEDGE surface forming 2 layers and 46 layers, respectively. In contrast, the small quantities of FQ and CQ adsorbed are not enough to completely cover the HEDGE area forming a layer.

11. Molecular dynamics simulation and DFT calculations. To account for orientation of the carbon electrode, we built carbon structures with different degree of graphitization. To reproduce the defects of graphite exposed in its $(01\bar{1}0)$ orientation, we have reproduced graphite-like structures using Tersoff potential and DFT geometry optimizations, as described in the manuscript.

First, we constructed the initial supercells consisting of 200 atoms of carbon using an orthogonalized version of the hexagonal graphite lattice in order to expose the 'edge' structure. Since we are interested in the interaction of organic molecules, such as quinones, with different morphologies of carbon electrodes, we explored the adsorption energies of quinones over three types of graphite-like structures.

The construction of the graphite-like structures is the following, we first use a melting-quenching-annealing schedule using NVT molecular dynamics with Nose-Hoover thermostat and Tersoff many body potential, using a previously reported methodology.[9] To account for porous carbon, we simulated in a low-density regime. We used densities from 0.50 to 0.9 g cm^{-3} in steps

of 0.04 g cm^{-3}, due to this region's high surface area carbon structure. These structures were constructed as orthogonal versions of the hexagonal lattices in order to expose the edge AB stacking of the graphite-like structure, that is, we want to reproduce the defects of graphite exposed in its $(01\bar{1}0)$ orientation.

The simulated carbon materials were produced by a linear heating from 300 to 4000 K in 50000 time-steps of 1 fs in duration, using NVT molecular dynamics and the Noose-Hoover thermostat, implemented in LAMMPS software. We have decided to test three different quenching rates, 0.03 K fs^{-1}, 0.05 K fs^{-1}, and 0.08 K fs^{-1} to get a total of 33 carbon samples (eleven densities and three quenching rates) with different atomic environments due to density and quenching rates. This procedure gave us nanoporous structures with different degree of graphitization and different orientations. All these structures were geometry optimized using the QuantumESPRESSO (QE) package. We have used no spin-polarized calculations and the GGA Burke-Perdew-Ernzehof exchange and correlation functional with VDW-DF dispersion correction functionals. We also used Ultrasoft-scalar-relativistic- pseudopotentials generated by the Rappe-Rabe-Kaxiras-Joannopoulos methodology. We have set the cut-off energy for the plane waves at 55 Ry (748 eV). For the convergence of the optimizations, the force and energy thresholds in the BFGS routine were 10^{-4} Ha/a_0 (5.14 x 10^{-3} eV $Å^{-1}$) and 10^{-6} eV, respectively. The Γ-point was used for the reciprocal space integration due to the lack of symmetry in real space. In figure S10a we have schematized the process for the production of the carbon structures.

We chose three possible geometries among the carbon structures generated: graphene-like structure, exposed edge structure (HEDGE), and amorphous-like structure (see Figure S10b). The characterization of these structures was performed using radial distribution functions, as can be seen from Figure S10b; both graphene-like structure and HEDGE show graphite like peaks due to graphene sheets at 2.8 and 3.7 Å. The amorphous-like carbon does not show that structure, suggesting a more amorphous structure than graphene-like structure and HEDGE. The simulated amorphous structure shows sp^2 and sp^3 bonded carbons in a randomly dispersed network. The simulated graphene-like structure shows a higher graphitization level, where the carbon atoms are mostly sp^2-bonded. This structure is mostly sheets of hexagons with some pentagons and octagons. Similarly, HEDGE structure also shows sheets of sp^2 bonded carbons, however a large number of edge sites can be visualized.

After the construction of the carbon structures, in order to produce a material more similar to the experimental conditions, some oxygen functionalities, such as carbonyl and hydroxyl functional groups, were introduced in the structure. For that, C-C bounds in HEDGE were broken, and oxygen and hydrogen atoms were added in the previously simulated HEDGE structure. Finally, the structure with oxygenated-functional groups was geometry optimized using the electronic parameters used in the previous simulations.

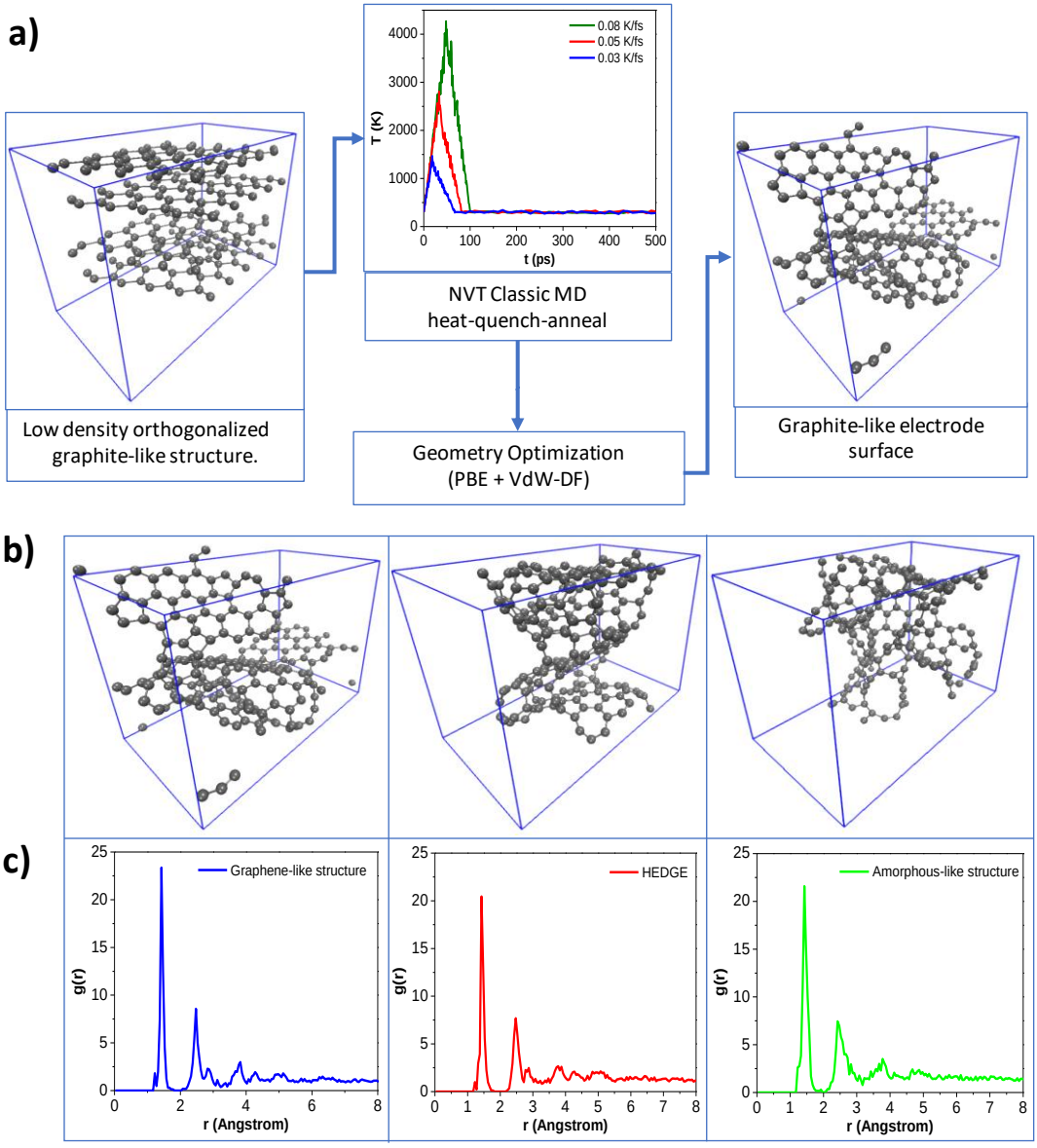

Figure S10. (a) Simulation process to generate the carbon electrode surfaces with some degree of graphitization. (b) Example of the three different degrees of graphitization using RDF. (c) radial distribution functions of graphene-like structure, HEDGE and amorphous-like structure.

The geometries of the four quinones were constructed and optimized using the Merck Molecular Forcefield (MMFF94) in order to find the lowest energy conformer of each quinone. These conformers were geometry-optimized using QE and the same parameters were used in the optimizations of the carbon structures. The HEDGE samples, both oxidized and not oxidized, have a complex geometry in which finding suitable places for docking becomes a difficult task in terms from both a geometric, and theoretical point of view. For this reason, we have used a classical potentials based docking code, SMINA,[10] to find the best docking positions of the molecules on the carbon surface. Once we find these docking positions, we proceed to calculate the adsorption energies by DFT geometry optimization calculations, Equation S6:

$$\Delta E_{ads} = E_{G+M} - E_G - E_M \qquad \text{(Equation S6)}$$

where E_{G+M} is geometry-optimized energy of the carbon surface with the molecule docked over it, E_M is the geometry-optimized isolated molecule inside the simulation box, and E_G is the geometry-optimized energy of carbon surface in the simulation box. The geometry optimizations have the same simulation parameters and the same size of the simulation box. ΔE_{ads} shows an attractive interaction between the surface and molecule, and has a magnitude on the order of kcal mol^{-1}.

12. HEDGE without oxygenated functional groups. We performed the same computational simulation and calculations with a HEDGE structure without oxygen-containing functional groups (HEDGE-nO) using the same electronic parameters used in the oxidized HEDGE structures in order to observe the behavior of the adsorption energy as oxygen functional groups are added to the carbon surface.

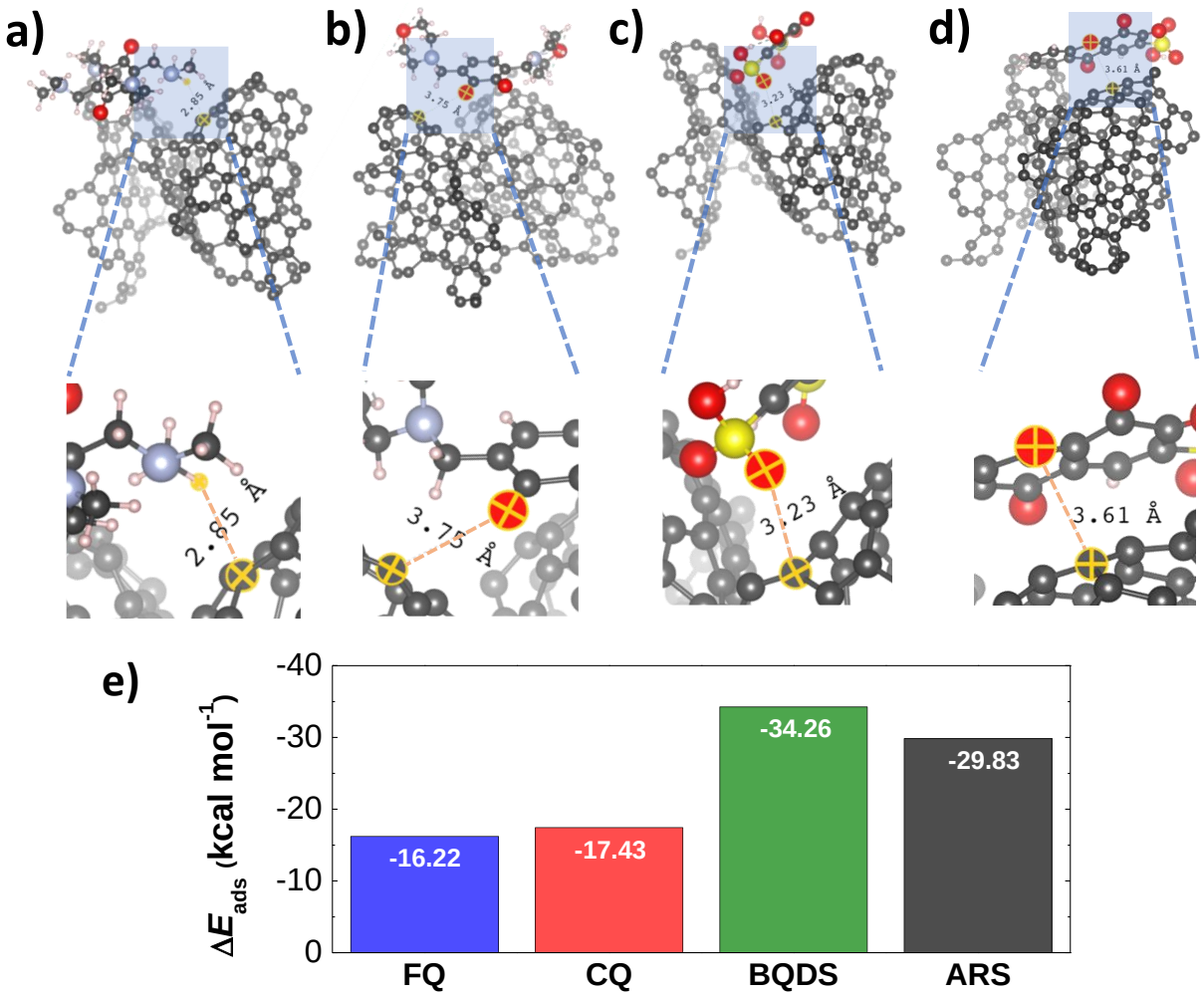

Figure S11. Lowest energy configurations of the fully-oxidized form of ARS (a), BQDS (b), CQ (c) and FQ (d) on HEDGE-nO surface. The arrows indicate edge sites with which the quinone-based compound interacts; gray, white, yellow, red and blue spheres represent carbon, hydrogen, sulfur, oxygen and nitrogen atoms, respectively. (e) Calculated ΔE_{ads} of each compound on HEDGE-nO.

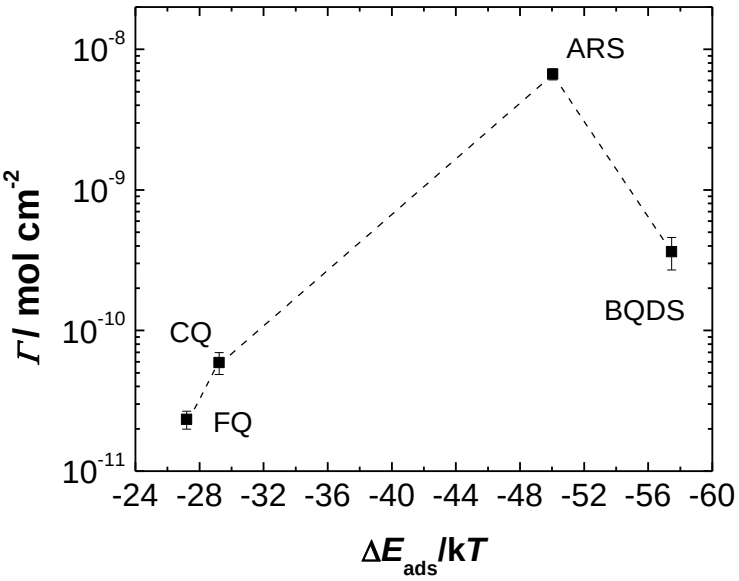

Figure S12. Surface excess vs. calculated $\Delta E_{\mathrm{ads}}/\mathrm{k}T$ (T = 300 K) for each quinone on HEDGE-nO.

References

(1) Park, M.; Beh, E. S.; Fell, E. M.; Jing, Y.; Kerr, E. F.; De Porcellinis, D.; Goulet, M.-A.; Ryu, J.; Wong, A. A.; Gordon, R. G.; et al. A High-Voltage Aqueous Zinc-Organic Hybrid Flow Battery. *Adv. Energy Mater.* **2019**, *9*, 1900694.

(2) Imai, K.; Nakanishi, I.; Ohno, A.; Kurihara, M.; Miyata, N.; Matsumoto, K. I.; Nakamura, A.; Fukuhara, K. Synthesis and Radical-Scavenging Activity of a Dimethyl Catechin Analogue. *Bioorganic Med. Chem. Lett.* **2014**, *24* (11), 2582–2584.

(3) Bard, A. J.; Faulkner, L. R. *Electrochemical Methods: Fundamentals and Applications*; 2001; Vol. 8.

(4) Bukalov, S. S.; Zubavichus, Y. V.; Leites, L. A.; Sorokin, A. I.; Kotosonov, A. S. Structural Changes in Industrial Glassy Carbon As a Function of Heat Treatment Temperature According To Raman Spectroscopy and X-Ray. *Nanosyst. Physics, Chem. Math.* **2014**, *5* (1), 186–191.

(5) Blyth, R. I. R.; Buqa, H.; Netzer, F. P.; Ramsey, M. G.; Besenhard, J. O.; Golob, P.; Winter, M. XPS Studies of Graphite Electrode Materials for Lithium Ion Batteries. *Appl. Surf. Sci.* **2000**, *167*, 99–106.

(6) Khalid, M.; Hassan, A.; Honorato, A. M. B.; Crespilho, F. N.; Varela, H. Nano-Flocks of Bimetallic Organic Framework for Efficient Hydrogen Evolution Electrocatalysis. *Chem. Commun.* **2018**, *54*, 11048–11051.

(7) Zou, Y.; Walton, A. S.; Kinloch, I. A.; Dryfe, R. A. W. Investigation of the Differential Capacitance of Highly Ordered Pyrolytic Graphite as a Model Material of Graphene Investigation of the Differential Capacitance of Highly Ordered Pyrolytic Graphite as a Model Material of Graphene. *Langmuir* **2016**, *32*, 11448.

(8) Zhao, L.; Wu, G.; Cai, Z.; Zhao, T.; Yao, Q.; Chen, X. Ultrasensitive Non-Enzymatic Glucose Sensing at near-Neutral PH Values via Anodic Stripping Voltammetry Using a Glassy Carbon Electrode Modified with Pt3Pd Nanoparticles and Reduced Graphene Oxide. *Microchim. Acta* **2015**, *182* (11–12), 2055–2060.

(9) Mejía-Mendoza, L. M.; Valdez-Gonzalez, M.; Muñiz, J.; Santiago, U.; Cuentas-Gallegos, A. K.; Robles, M. A Theoretical Approach to the Nanoporous Phase Diagram of Carbon. *Carbon* **2017**, *120*, 233–243.

(10) Koes, D. R.; Baumgartner, M. P.; Camacho, C. J. Lessons Learned in Empirical Scoring with Smina from the CSAR 2011 Benchmarking Exercise. *J. Chem. Inf. Model.* **2013**, *53* (8), 1893–1904.